A Dynamically Weighted Constrained Complete Active Space Ansatz for Constructing Multiple Potential Energy Surfaces Within the Anderson-Holstein Model

Junhan Chen and Joseph Subotnik*

Department of Chemistry, University of Pennsylvania, Philadelphia, Pennsylvania 19104, USA

E-mail: subotnik@sas.upenn.edu

Phone: +1 (215) 746-7078

Abstract

We derive and implement the necessary equations for solving a dynamically weighted, state-averaged constrained CASSCF(2,2) wavefunction describing a molecule on a metal surface. We show that a partial constraint is far more robust than a full constraint. We further calculate the system-bath electronic couplings that arise because, near a metal, there is a continuum (rather than discrete) number of electronic states. This approach should be very useful for simulating heterogeneous electron transfer going forward.

I Introduction

Molecular dynamics at metal surfaces is a fascinating research area. From a theoretical perspective, there are just so many processes of interest: fast molecular scattering,[1–5] slow electrochemical dynamics (e.g. molecular junctions[6–15]), electron transfer,[16–20] vibrational dissipation,[21,22] and electron-hole creation.[23,24] Of course, all of these processes can couple to photons (e.g. photo-electrochemistry[25]) or to protons (i.e. heterogeneous proton-coupled electron transfer[26]). From an experimental point of view, all of the above can be studied, even though it is difficult to separate the different effects.

In the present article, our interest is in the area of non-adiabatic dynamics and the question of how to propagate nuclear dynamics for molecules when electron transfer is possible. The phenomenon of interfacial electron transfer at a metal surface lies at the heart of Marcus's electrochemical rate theory[27] and in recent years our research group[28–31] and others have made a broad push to model such dynamics semiclassically (as applicable to large systems). While quite a bit of progress has been made to date, the inevitable practical problem that arises is not of a *dynamical* nature but rather of an *electronic structure* nature. How can we best (and most quickly) describe the electronic wavefunction of a molecule at an interface, especially if there is strong molecule-metal coupling? The usual frameworks would be GW methods,[32–34] embedding methods,[35–38] constrained DFT,[39–46] and/or ΔSCF.[47] That being said, recently[48] we introduced an orthogonal approach. Namely, we showed early data suggesting that a small CASSCF(2,2) calculation (if properly constrained) could function as an excellent method, balancing accuracy and computational speed. The key insight presented in Ref. 48 is that, when constructing such a CASSCF(2,2) approach, one must be sure (*i*) to constrain the two active orbitals so that their total population has some overlap with the molecule on the surface; and (*ii*) to use state-averaging so as to balance the gap between the ground and excited state and make smooth surfaces. If one implements these guidelines, Ref. 48 demonstrates that the resulting algorithm can seemingly perform quite well (at least for those models tested).

With this background in mind, in the present paper, we have three goals in mind. First, because the molecular constraint just described above [(i)] is highly non-standard, we will show how to derive the necessary equations (and we will further analyze other possible constraints). Second, for the sake of completeness, we will then provide step-by-step instructions delineating exactly how to solve the equations just described, and we will benchmark the convergence of our proposed optimization. Third and finally, going beyond Ref. 48, we will investigate the couplings to the bath that arise from the infinite continuum of states. These couplings are needed if we wish to run fully nonadiabatic dynamics that are compatible with Marcus's electrochemical rate expression and achieve electronic equilibration to the correct temperature, e.g. as in the FSSH-ER[31] dynamics.

II Theory

We will now present the relevant equations as far as determining a constrained CASSCF(2,2) solution for an impurity on a metallic substrate.

A Review of CASSCF(2,2) Theory

To implement a constrained CASSCF theory, we must establish the necessary nomenclature conventions. Henceforward, we let i, j represent inactive (i.e. fully occupied) orbitals; t, u, v, w, x, y represent active orbitals; a represent an (empty) virtual orbital; and m, n, p, q, r, s represent arbitrary orbitals. Clearly, the identity can be resolved as

$$\hat{I} = \hat{P}_{inactive} + \hat{P}_{active} + \hat{P}_{virtual} \tag{1}$$

where $\hat{P}_{inactive}, \hat{P}_{active}$ and $\hat{P}_{virtual}$ are projection operators onto the inactive, active, and virtual orbitals. Subscripts α, β index electronic spin. p_α refers to a spin orbital while p refers to a spatial orbital. We index atomic orbitals with greek letters μ and ν.

We will now give a very brief review of CASSCF following Ref. 49(Helgaker). The savvy reader familiar with the CASSCF formalism can skip directly to Sec. B.

We consider a spin-conserving Hamiltonian in second quantization,

$$\begin{aligned} H = & \sum_{pq} \sum_{\alpha} h_{p_\alpha q_\alpha} p_\alpha^\dagger q_\alpha \\ & + \frac{1}{2} \sum_{pqrs} \sum_{\alpha\beta} g_{p_\alpha q_\alpha r_\beta s_\beta} p_\alpha^\dagger r_\beta^\dagger s_\beta q_\alpha \end{aligned} \tag{2}$$

Because we do not include spin-orbit coupling, the one electron Hamiltonian does not depend on spin:

$$h_{p_\alpha q_\alpha} = h_{pq} \tag{3}$$

The two electron integrals are written in chemists' notation

$$\begin{aligned} g_{mnpq} &= (mn|pq) \\ &= \int \frac{\phi_m^*(\boldsymbol{r_1})\phi_n(\boldsymbol{r_1})\phi_p^*(\boldsymbol{r_2})\phi_q(\boldsymbol{r_2})}{|\boldsymbol{r_1} - \boldsymbol{r_2}|} d\boldsymbol{r_1} d\boldsymbol{r_2} \end{aligned} \tag{4}$$

with the following symmetries:

$$g_{pqrs} = g_{p_\alpha q_\alpha r_\beta s_\beta} \tag{5}$$

A simple calculations shows that the total energy (i.e. the expectation value of Hamiltonian) can be written as:

$$\langle H \rangle = \sum_{pq} h_{pq} D_{pq} + \frac{1}{2} \sum_{pqrs} g_{pqrs} \tilde{D}_{pqrs} \tag{6}$$

where the one-particle D_{mn} and two-particle $\tilde{D}_{mnpq}$ density matrices are defined as:

$$\begin{aligned} D_{pq} &= \sum_{\alpha} \langle 0 | p_\alpha^\dagger q_\alpha | 0 \rangle \\ \tilde{D}_{pqrs} &= \sum_{\alpha\beta} \langle 0 | p_\alpha^\dagger r_\beta^\dagger s_\beta q_\alpha | 0 \rangle \end{aligned} \tag{7}$$

where $|0\rangle$ represents the multi-configurational ground state.

Following Ref. 49, the total electronic energy can be written using the (non-Hermitian) generalized Fock matrix F and the one electron density matrix D:

$$E = \frac{1}{2}\sum_{pq}(D_{pq}h_{pq} + \delta_{pq}F_{pq}). \tag{8}$$

Here, the generalized Fock matrix is defined as:

$$F_{mn} = \sum_{\alpha} \langle 0|m_{\alpha}^{\dagger}[n_{\alpha}, \hat{H}]|0\rangle \tag{9}$$

which is equivalent to:

$$\begin{aligned} F_{mn} &= \sum_{q} D_{mq}h_{nq} + \sum_{qrs} \tilde{D}_{mqrs}g_{nqrs} \\ &= \sum_{q} D_{mq}h_{nq} + \sum_{qrs} \tilde{D}_{rsmq}g_{rsnq}, \end{aligned} \tag{10}$$

In the above equation, the second equality uses the relationship:

$$\begin{aligned} \tilde{D}_{mqrs} &= \tilde{D}_{rsmq} \\ g_{mqrs} &= g_{rsmq} \end{aligned} \tag{11}$$

For real orbitals, one can switch $\{mn\}$ or $\{pq\}$, i.e.:

$$g_{mnpq} = g_{nmpq} = g_{mnqp} = g_{nmqp} \tag{12}$$

To calculate general Fock matrix F_{mn}, there are three different cases for the row index m:

1. If the first index is inactive i and the second index is any orbital n:

$$\begin{aligned} F_{in} &= \sum_q D_{iq} h_{nq} + \sum_{qrs} \tilde{D}_{rsiq} g_{rsnq} \\ &= 2h_{ni} + \sum_{qrs} (2\delta_{iq} D_{rs} - \delta_{si} D_{rq}) g_{rsnq} \\ &= 2h_{ni} + \sum_{rs} D_{rs} (2g_{rsni} - g_{rins}) \\ &= 2({}^I F_{ni} + {}^A F_{ni}) \end{aligned} \tag{13}$$

Here the second equality uses the relationship:

$$\begin{aligned} D_{iq} &= 2\delta_{iq} \\ \tilde{D}_{rsiq} &= 2\delta_{iq} D_{rs} - \delta_{si} D_{rq}, \end{aligned} \tag{14}$$

and the so-called inactive ${}^I F$ and active ${}^A F$ Fock matrices are defined as:

$$\begin{aligned} {}^I F_{mn} &= h_{mn} + \sum_j (2g_{mnjj} - g_{mjjn}) \\ {}^A F_{mn} &= \sum_{vw} D_{vw} (g_{mnvw} - \frac{1}{2} g_{mwvn}) \end{aligned} \tag{15}$$

2. When the first index is active v and the second index is any orbital n:

$$F_{vn} = \sum_q D_{vq} h_{nq} + \sum_{qrs} \tilde{D}_{vqrs} g_{nqrs} \tag{16}$$

$$= \sum_w D_{vw} h_{nw}$$

$$+ \sum_{iqs} \tilde{D}_{vqis} g_{isnq} + \sum_{wqs} \tilde{D}_{vqws} g_{wsnq} \tag{17}$$

$$= \sum_w D_{vw} h_{nw} + \sum_{wi} D_{vw} (2 g_{iinw} - g_{iwni})$$

$$+ \sum_{wxy} \tilde{D}_{vxwy} g_{wynx} \tag{18}$$

$$= \sum_w {}^I F_{nw} D_{vw} + Q_{vn} \tag{19}$$

In going from Eq. 16 to 17, we change from the arbitrary index q to the active index w because only D_{vw} is non-zero (i.e. D_{vi} and D_{va} are always zero). Between Eq. 16 and 17, we separate the sum over an arbitrary index r into a sum over an inactive index i and an active index w as far as the $\tilde{D}_{vqrs}$ term is concerned. Between Eq. 17 and Eq. 18, we then recognize that $\tilde{D}_{vqws}$ is nonzero only when q, s are active, so that in Eq. 18, we have replaced q, s with x, y. In Eq. 19, we have introduced the auxiliary Q matrix:

$$Q_{vm} = \sum_{wxy} \tilde{D}_{vwxy} g_{mwxy} \tag{20}$$

3. Finally, when the first index is virtual a, the general Fock matrix vanishes:

$$F_{an} = 0 \tag{21}$$

Finally, all that remains is calculate the density matrices D_{vw} and $\tilde{D}_{vwxy}$ where all indices are active. Note that, for a CASSCF calculation, we have only two active orbitals, which henceforward we label t, u; we envision t to be the orbital with lower energy and u to

be the orbital with higher energy. Ignoring the core (inactive) orbitals, the CASSCF(2,2) wavefunction $|\Psi_0\rangle$ can be written as:

$$|\Psi_0\rangle = \alpha\,|t\bar{t}\rangle + \beta\,|u\bar{u}\rangle + \gamma(|t\bar{u}\rangle + |u\bar{t}\rangle) \tag{22}$$

We then can evaluate the one-particle density matrix (1PDM):

$$\begin{aligned} D_{tt} &= 2(\alpha^2 + \gamma^2) \\ D_{tu} &= D_{ut} = 2(\alpha + \beta)\gamma \\ D_{uu} &= 2(\beta^2 + \gamma^2) \end{aligned} \tag{23}$$

As one would expect, the trace of the 1PDM is the number of active electrons:

$$2 = D_{uu} + D_{tt} = 2(\alpha^2 + \beta^2 + 2\gamma^2) \tag{24}$$

Next, for two-particle density matrix (2PDM), we find:

$$\begin{aligned} \tilde{D}_{tttt} &= 2\alpha^2 \\ \tilde{D}_{tttu} &= \tilde{D}_{ttut} = \tilde{D}_{tutt} = \tilde{D}_{uttt} = 2\alpha\gamma \\ \tilde{D}_{ttuu} &= \tilde{D}_{uutt} = \tilde{D}_{uttu} = \tilde{D}_{tuut} = 2\gamma^2 \\ \tilde{D}_{tutu} &= \tilde{D}_{utut} = 2\alpha\beta \\ \tilde{D}_{tuuu} &= \tilde{D}_{utuu} = \tilde{D}_{uutu} = \tilde{D}_{uuut} = 2\beta\gamma \\ \tilde{D}_{uuuu} &= 2\beta^2 \end{aligned} \tag{25}$$

A.1 Final Form for the Gradient

Finally, we can write down the electronic gradient. A CASSCF ansatz is a function of coefficients and orbital rotations. The gradients with respect to coefficients are easy to extract; one merely diagonalizes the Hamiltonian for a fixed set of orbitals. As far as the

optimization of the orbitals is concerned, as for any CASSCF calculation, there are 6 classes of orbital rotations (see a schematic matrix below):

$$\begin{bmatrix} (\kappa_{ji}) & \kappa_{it} & \kappa_{ia} \\ \kappa_{ti} & (\kappa_{ut}) & \kappa_{ta} \\ \kappa_{ai} & \kappa_{at} & (\kappa_{ba}) \end{bmatrix} \tag{26}$$

However, note that all intraspace rotations (e.g. κ_{ji},κ_{ut} and κ_{ba}) are redundant. Thus, we need to evaluate the electronic energy gradient only with respect to the inactive-active rotations κ_{it}, the inactive-virtual rotations κ_{ia} and the active-virtual rotations κ_{ta}. Following Ref. 49, the electronic gradient can be written as

$$B_{mn} = 2 \langle 0|[E_{mn}, \hat{H}]|0\rangle \,, \tag{27}$$

where the orbital excitation operator E_{mn} is defined as:

$$E_{mn} = \sum_{\alpha} m_{\alpha}^{\dagger} n_{\alpha} \tag{28}$$

Using basic algebra, B_{mn} can be re-expressed as:

$$\begin{aligned} B_{mn} = 2 \sum_{\alpha} [& \langle 0|m_{\alpha}^{\dagger}[n_{\alpha}, \hat{H}]|0\rangle \\ & - \langle 0|n_{\alpha}^{\dagger}[m_{\alpha}, \hat{H}]|0\rangle] \qquad (29) \\ = 2(F_{mn} & - F_{nm}), \qquad (30) \end{aligned}$$

Henceforward, the final electronic energy gradient expression is:

$$
\begin{aligned}
B_{it} &= \frac{\partial E}{\partial \kappa_{it}} \\
&= 2(F_{it} - F_{ti}) \\
&= 2(2^I F_{ti} + 2^A F_{ti} - \sum_w {}^I F_{iw} D_{tw} - \sum_{wxy} \tilde{D}_{twxy} g_{iwxy}) \\
&= 2\{2[h_{ti} + \sum_j (2g_{tijj} - g_{tjji})] + 2[\sum_{vw} D_{vw}(g_{tivw} - \frac{1}{2} g_{tvwi})] \\
&- \sum_w [h_{iw} + \sum_j (2g_{iwjj} - g_{ijjw})] D_{tw} - \sum_{wxy} \tilde{D}_{twxy} g_{iwxy}\}
\end{aligned}
\tag{31}
$$

$$
\begin{aligned}
B_{ia} &= \frac{\partial E}{\partial \kappa_{ia}} \\
&= 2(F_{ia} - F_{ai}) \\
&= 2(2^I F_{ai} + 2^A F_{ai}) \\
&= 2\{2[h_{ai} + \sum_j (2g_{aijj} - g_{ajji})] + 2[\sum_{vw} D_{vw}(g_{aivw} - \frac{1}{2} g_{avwi})]\}
\end{aligned}
\tag{32}
$$

$$
\begin{aligned}
B_{ta} &= \frac{\partial E}{\partial \kappa_{ta}} \\
&= 2(F_{ta} - F_{at}) \\
&= 2(\sum_w {}^I F_{aw} D_{tw} + \sum_{wxy} \tilde{D}_{twxy} g_{awxy}) \\
&= 2\{\sum_w [h_{aw} + \sum_j (2g_{awjj} - g_{ajjw})] D_{tw} + \sum_{wxy} \tilde{D}_{twxy} g_{awxy}\}
\end{aligned}
\tag{33}
$$

B State-Averaged Constrained CASSCF(2,2) Energy and Gradient

In Ref. 48, we analyzed the Anderson Hamiltonian, which can be written as:

$$\begin{aligned}
\hat{H}_{el} &= \frac{1}{2}m\omega^2 x^2 + \hat{H}_{one}(x) + \hat{\Pi} \\
\hat{H}_{one}(x) &= \epsilon_{d_1}(x)\sum_{\sigma} d^{\dagger}_{1\sigma}d_{1\sigma} + \epsilon_{d_2}(x)\sum_{\sigma} d^{\dagger}_{2\sigma}d_{2\sigma} \\
&+ t_d \sum_{\sigma}(d^{\dagger}_{1\sigma}d_{2\sigma} + d^{\dagger}_{2\sigma}d_{1\sigma}) \\
&+ \sum_{k\sigma}\epsilon_{k\sigma}b^{\dagger}_{k\sigma}b_{k\sigma} + \sum_{k\sigma} V_k(d^{\dagger}_{1\sigma}b_{k\sigma} + b^{\dagger}_{k\sigma}d_{1\sigma}) \\
\hat{\Pi} &= U(d^{\dagger}_{1\uparrow}d_{1\uparrow}d^{\dagger}_{1\downarrow}d_{1\downarrow} + d^{\dagger}_{2\uparrow}d_{2\uparrow}d^{\dagger}_{2\downarrow}d_{2\downarrow}) \\
\epsilon_{d_1}(x) &= e_{d_1} - \sqrt{2}gx \\
\epsilon_{d_2}(x) &= e_{d_2} - \sqrt{2}gx
\end{aligned} \tag{34}$$

Here, d_1 and d_2 are impurity atomic orbitals and $b_{k\sigma}$ is a bath atomic orbital with electronic orbital index k and spin σ. The Hamiltonian above is two-site impurity model (with d_1 and d_2); if one includes only d_1, the Hamiltonian becomes a one-site model. The impurity-bath couplings are characterized by a hybridization function:

$$\Gamma(\epsilon) = \sum_{k} |V_k|^2 \delta(\epsilon_k - \epsilon) \tag{35}$$

For the results below, we will make the wide band approximation, so that $\Gamma(\epsilon) = \Gamma$ is independent of energy.

To study charge transfer between a molecule and a metal surface, the active space must be chosen carefully. In general, the 2 active orbitals t, u must be well-balanced mixtures of both the impurity atomic orbitals $\{d_\mu\}$ and the bath atomic orbitals $\{b_\nu\}$. We will not be able to recover charge transfer if the active orbitals are exclusively on the impurity or in the bath. Thus, a constraint becomes necessary if we wish to guarantee that we find such a

well-balanced mixture of orbitals from a CASSCF solution.

B.1 Form of the Constraint

Let us denote the projection onto the impurity as:

$$\hat{P}_{imp} = \sum_{\mu \in \mathbf{impurity}} d_\mu^\dagger d_\mu \tag{36}$$

and the projection onto the bath as:

$$\hat{P}_{bath} = \sum_{\nu \in \mathbf{bath}} b_\nu^\dagger b_\nu. \tag{37}$$

Clearly, one can write the identity as:

$$\hat{I} = \hat{P}_{imp} + \hat{P}_{bath} \tag{38}$$

One possible constraint enforcing this active orbital requirement is insisting on a total population on the impurity for the active space:

$$\begin{aligned} &\mathrm{Tr}_{active}\left(\hat{P}_{imp}\right) \\ &= \sum_{\mu \in \mathbf{impurity}} \langle t|d_\mu^\dagger d_\mu|t\rangle + \langle u|d_\mu^\dagger d_\mu|u\rangle = 1 \end{aligned} \tag{39}$$

Because

$$\langle t|t\rangle + \langle u|u\rangle = 2, \tag{40}$$

Eq. 39 is equivalent to

$$\begin{aligned} &\mathrm{Tr}_{active}\left(\hat{P}_{bath}\right) \\ &= \sum_{\mu \in \mathbf{bath}} \langle t|b_\mu^\dagger b_\mu|t\rangle + \langle u|b_\mu^\dagger b_\mu|u\rangle = 1 \end{aligned} \tag{41}$$

In other words, constraining the impurity is equivalent to constraining the bath. Hencefor-

ward, we will label this a "partial constraint" ("pc" for short).

Below, we will compare Eqn. 39 against a stricter "full constraint" ("fc" for short), where we insist that each of two active orbitals is fully localized on either the impurity or bath (resulting in two [not one] constraints):

$$\begin{aligned} \sum_{\mu \in \mathbf{impurity}} \langle t | d_\mu^\dagger d_\mu | t \rangle &= 1; \\ \sum_{\mu \in \mathbf{impurity}} \langle u | d_\mu^\dagger d_\mu | u \rangle &= 0 \end{aligned} \tag{42}$$

Although the derivation below is given for the case of a partial constraint, the electronic energy and gradient has a straightforward analogy for the case of the full constraint.

B.2 The Need for State Averaging

As discussd above, without the constraints above, a CASSCF(2,2) calculation could easily produce two active orbitals localized to the bath, which would not help in describing the molecule-metal charge transfer problem. Thus, the constraints above are *necessary*. That being said, these constraints are not yet *sufficient* as far generating a balanced set of active orbitals; one still must perform a state-average CASSCF(2,2) to get meaningful excited states.

To see why a state average is absolutely essential, consider a single site Anderson model without the onsite repulsion U and the limiting case where the the impurity site is fully occupied for the ground state, i.e. $\left\langle d^\dagger d \right\rangle = \left\langle \bar{d}^\dagger \bar{d} \right\rangle = 1$. In such a case, the ground state CASSCF(2,2) $|\Psi_0\rangle$ can be written as (ignoring the core electrons);

$$|\Psi_0\rangle = \left| d\bar{d} \right\rangle, \tag{43}$$

and there is no stable means to identify the corresponding active orbital in the bath, b. In other words, without state averaging, b is chosen as that orbital that most helps to lower

the energy of the ground state; however, in this regime, the ground state really does not mix with the bath and so the choice of b will be numerically unstable. As a result, as we change the fermi level, we will likely see instabilities of the excited states. Indeed, these instabilities will be shown below. Note that this unstable structure can be easily removed, however, if we simply give some weight to the excited state so that the latter is chosen robustly. For this reason, we will perform state-averaging below.

For this reason, we will now explicitly write down the energy and gradient expression for state-averaged constrained CASSCF(2,2). First, we write out the three CASSCF(2,2) states:

$$|\Psi_0\rangle = \alpha_0 |t\bar{t}\rangle + \beta_0 |u\bar{u}\rangle + \gamma_0 |t\bar{u} + u\bar{t}\rangle \tag{44}$$

$$|\Psi_1\rangle = \alpha_1 |t\bar{t}\rangle + \beta_1 |u\bar{u}\rangle + \gamma_1 |t\bar{u} + u\bar{t}\rangle \tag{45}$$

$$|\Psi_2\rangle = \alpha_2 |t\bar{t}\rangle + \beta_2 |u\bar{u}\rangle + \gamma_2 |t\bar{u} + u\bar{t}\rangle \tag{46}$$

The state-averaged CASSCF(2,2) energy can be written as:

$$E^{SA-CASSCF(2,2)} = \sum_{I=0}^{2} w_I \langle I|H|I\rangle , \tag{47}$$

where w_I is the weight for the energy of Ith CASSCF(2,2) state. For reasonable ground and excited states– both near and far from crossing regimes – we employ dynamically weighted weights of the form:[50]

$$\begin{aligned} w_0 &= \frac{1}{1 + e^{-\zeta(E_1 - E_0)} + e^{-\zeta(E_2 - E0)}} \\ w_1 &= \frac{e^{-\zeta(E_1 - E_0)}}{1 + e^{-\zeta(E_1 - E_0)} + e^{-\zeta(E_2 - E0)}} \\ w_2 &= \frac{e^{-\zeta(E_2 - E0)}}{1 + e^{-\zeta(E_1 - E_0)} + e^{-\zeta(E_2 - E0)}}. \end{aligned} \tag{48}$$

For this exponential weighting factors, the parameter ζ controls the mixing strength of the ground state with the excited states. When $\zeta \to 0$, we recover three-state-averaged CASSCF(2,2) with equal weighting $w_I = \frac{1}{3}$; when $\zeta \to \infty$, we recover becomes state-specific

CASSCF(2,2).

$$\begin{cases} \zeta \to 0 & \text{equal weighting} \\ \zeta \to \infty & \text{ground-state-specific} \end{cases} \tag{49}$$

Compared to the state-specific CASSCF(2,2) energy in Eq. 6, the state-averaged CASSCF(2,2) energy is different only in the way we construct the state-averaged 1PDM and 2PDM:

$$\begin{aligned} D_{pq} &= \sum_{I=0}^{2} w_I D_{pq}^I \\ \tilde{D}_{pqrs} &= \sum_{I=0}^{2} w_I \tilde{D}_{pqrs}^I. \end{aligned} \tag{50}$$

Here, the state-specific 1PDM D_{pq}^I and 2PDM $\tilde{D}_{pqrs}^I$ in the active space basis are calculated in Eqs. 23 and 25.

B.3 Minimization with Lagrange Multipliers to Find a Solution

In order to obtain a state-averaged constrained CASSCF(2,2) solution, we look for stationary solutions of a lagrangian representing the state-averaged CASSCF(2,2) energy with the active orbital constraint:

$$\mathcal{L} = E^{SA-CASSCF(2,2)} - \lambda\{\sum_{\mu \in \textbf{impurity}} \langle t|d_\mu^\dagger d_\mu|t\rangle + \langle u|d_\mu^\dagger d_\mu|u\rangle - 1\}, \tag{51}$$

Here λ is the relevant lagrange multiplier for the constraint. Following Eqs. 31, 32 and 33), the analogous derivative of the lagrangian with respect to orbital rotations is:

$$\begin{aligned} \tilde{B}_{it} = 2\{2[h_{ti} + \sum_j (2g_{tijj} - g_{tjji})] + 2[\sum_{vw} D_{vw}(g_{tivw} - \frac{1}{2} g_{tvwi})] \\ - \sum_w [h_{iw} + \sum_j (2g_{iwjj} - g_{ijjw})] D_{tw} - \sum_{wxy} \tilde{D}_{twxy} g_{iwxy}\} \\ + 2\lambda \sum_{\mu \in \textbf{impurity}} \langle i|d_\mu^\dagger d_\mu|t\rangle \end{aligned} \tag{52}$$

$$\tilde{B}_{ia} = 2\{2[h_{ai} + \sum_j (2g_{aijj} - g_{ajji})] + 2[\sum_{vw} D_{vw}(g_{aivw} - \frac{1}{2}g_{avwi})]\} \tag{53}$$

$$\begin{aligned}\tilde{B}_{ta} = 2\{&\sum_w [h_{aw} + \sum_j (2g_{awjj} + g_{ajjw})]D_{tw} + \sum_{wxy} \tilde{D}_{twxy} g_{awxy}\} \\ &- 2\lambda \sum_{\mu \in \textbf{impurity}} \langle t|d_\mu^\dagger d_\mu|a\rangle\end{aligned} \tag{54}$$

Therefore, applying a variational principle to the lagrangian in Eq. 51 is equivalent to solving a set of self-consistent equations given by Eq. 39 and Eq. 55:

$$(\hat{B} + \lambda \hat{V})\,|k\rangle = \epsilon_k\,|k\rangle \tag{55}$$

Here, $\hat{B}$ is the matrix in Eqs. 31, 32 and 33 and $\hat{V}$ is an operator that arises from the constraint:

$$\hat{V} = 2\,\left(\hat{P}_{inact}\hat{P}_{imp}\hat{P}_{active} + \hat{P}_{active}\hat{P}_{imp}\hat{P}_{inact} - \hat{P}_{virt}\hat{P}_{imp}\hat{P}_{active} - \hat{P}_{active}\hat{P}_{imp}\hat{P}_{virt}\right) \tag{56}$$

In practice, there are many means by which one can solve the equations above. In the present paper, we consider the optimization problem above (Eq. 51) as an equality-constrained quadratic optimzation problem and following standard optimization approaches,[51] we solve the relevant Newton-Karush–Kuhn–Tucker (Newton-KKT) matrix equations:

$$\begin{bmatrix} \boldsymbol{\nabla}^2_{xx}\mathcal{L}_k & -\boldsymbol{\nabla}C(x_k) \\ \boldsymbol{\nabla}C^T(x_k) & 0 \end{bmatrix} \begin{bmatrix} p_k \\ \lambda_{k+1} \end{bmatrix} = \begin{bmatrix} -\boldsymbol{\nabla}E^{SA-CASSCF(2,2)}(x_k) \\ -C(x_k) \end{bmatrix} \tag{57}$$

Here, $C(x_k)$ is the constraint (Eq. 39); x_k is a generic variable in the orbital rotation space (Eq. 26) for the k-th optimization cycle; p_k is the walking direction for x_k, i.e. $x_{k+1} = x_k + \alpha p_k$ and the step length α is obtained from a line search; λ_{k+1} is the lagrange multiplier for the next $(k+1)$-th optimization cycle. To reduce the computational cost, the hessian $\boldsymbol{\nabla}^2_{xx}\mathcal{L}$ is approximated and updated by a BFGS scheme.

III Details of the Implementation

We may summarise our implementation of DW-SA-cCASSCF(2,2) with the algorithm flowchart in Fig. 1. Note that this implementation should be valid for any reasonably sized impurity (larger than one site):[52]

- First, we calculate the 1PDM and 2PDM for our state-average target function (using Eq. 23, Eq. 25 and Eq. 50) with an initial set of weighting factors ($\omega_0 = 1, \omega_1 = 0, \omega_2 = 0$ in Eq. 48).

- Second, we solve the Newton-KKT equations 57 in order to optimize orbitals and the lagrange multiplier;

- Third, we diagonalize the configuration interaction (CI) Hamiltonian (3×3 for CAS(2,2)) and recover the CI coefficients.

- Finally, we examine the norm of the energy gradient in Eqs. 52, 53 and 54: if the gradient is smaller than a target threshold, the calculation has converged; otherwise, we update the weighting factor according to the Eq. 48 and repeat the whole procedure.

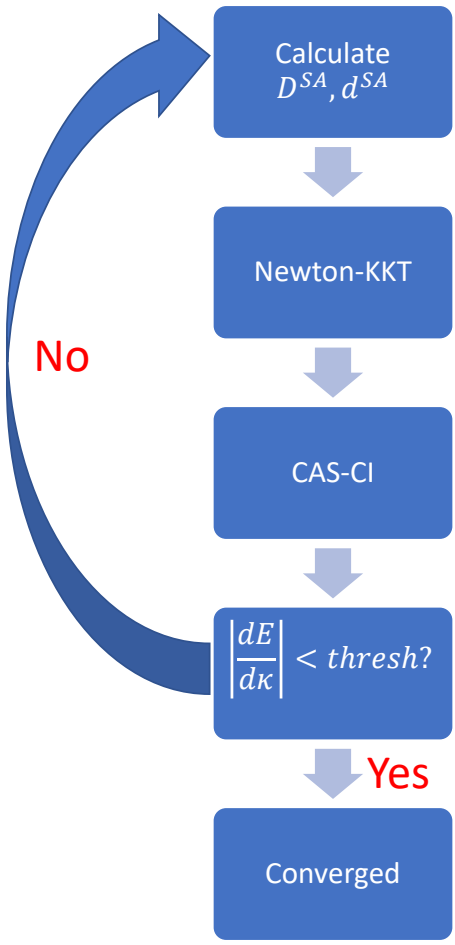

Figure 1: A flowchart of dynamically weighted state-averaged constrained CASSCF(2,2)

IV Results

We will now present three sets of data that allow for a better understanding of the above calculation (both theoretically and practically). First, we will present data as to the convergence performance of DW-SA-cCASSCF(2,2), studying different Γ with and without electron-electron interactions. Second, we will assess the choice of the dynamical weighting parameter ζ and show how the results vary with ζ. Third, we will compare results for a partially localized constraint (pc) versus a fully localized constraint (fc).

A Convergence

For the one-site calculations below, we start with such an initial guess: we use the identity matrix and switch its first column with the $\frac{Ne}{2}$-th column (Ne is the total number of electrons). The parameter set is: $m\omega^2 = 0.003, g = 0.0075, e_{d_1} = 0.05$, and we discretize the bath with 101 metallic states evenly distributed with energy spacing $dE = \frac{\Gamma}{10}$. We set the dynamical weighting parameter to be $\zeta = 40$. And we set the convergence threshold for the norm of gradient to be 1×10^{-4}. In Table 1 and Table 2, we report total number of orbital optimization cycles needed to converge the calculation. We observe that (i) convergence is harder when Γ is large; and (ii) converge is also more difficult when the electron-electron repulsion is finite ($U = 0.1$). Clearly, for $\Gamma = 0.01$, our algorithm for finding a cCASSCF solution is suboptimal and can be improved (the number in the bracket is calculated by reading the CI coeffcients for $\Gamma = 0.001$). Nevertheless, we have been able to converge the solutions and, as we show below, the final states are illuminating.

Table 1: Convergence Results for $U = 0$

Γ	1×10^{-2}	1×10^{-3}	1×10^{-4}	1×10^{-5}
Converging cycles	336(52)	3	3	2
Time(s)	54(12)	3	3	2

Table 2: Convergence Results for $U = 0.1$

Γ	1×10^{-2}	1×10^{-3}	1×10^{-4}	1×10^{-5}
Converging cycles	388(45)	3	3	3
Time(s)	117(10)	3	3	3

B Choice of ζ

In order to analyze the pros and cons of a given choice of ζ, we study three different criteria by which we can judge the resulting solutions focusing on the one-site model ($U = 0$):

1. One criterion is the ground state energy accuracy; for the case of $U = 0$, clearly an exact energy can be obtained for us to benchmark against.

2. A second criterion is the excited state energy asymptotic behavior. Here, we expect that a proper excited state should asymptotically approach the relevant diabatic energy when the impurity onsite energy is far away from the fermi level.

3. A third criterion is smoothness. For dynamics, it will be essential that we obtain smooth DW-SA-cCASSCF energies and wavefunctions.

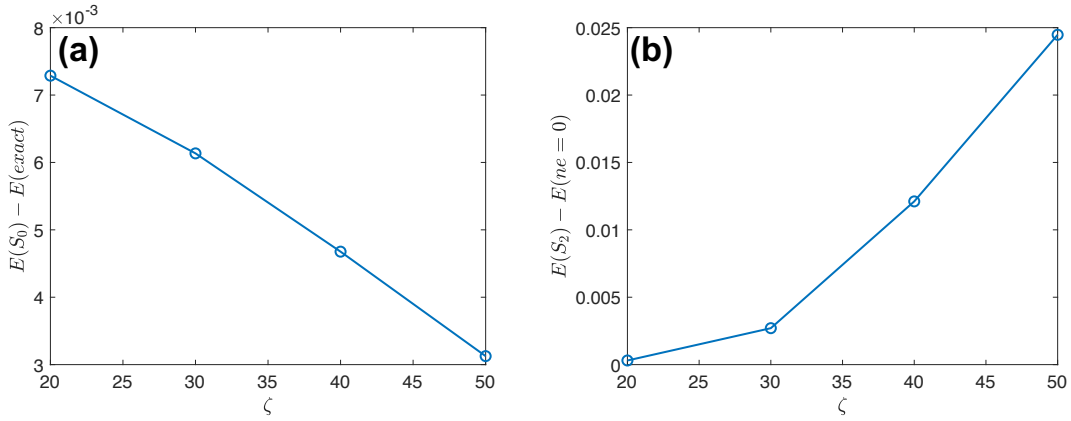

Figure 2: Different metrics for guiding the choice of ζ. (a) The ground state energy difference between the DW-SA-pcCASSCF(2,2) state S_0 and the exact ground state (the difference is measured at the curve crossing point); in general, we want the most accurate ground state energy possible. (b) The excited state energy difference between the DW-SA-pcCASSCF(2,2) state S_2 and the $ne = 0$ diabatic state (i.e. the diabatic state whose number of electrons on the impurity is 0). Far away from the crossing point, the onsite energy $\epsilon_d(x)$ is so much larger energy than the fermi level that for a good algorithm, the asymptotic behavior of the S_2 energy should approach the $ne = 0$ diabatic state energy. Note that these two metrics favor opposite ζ parameters, and so have we chosen $\zeta = 40$ as a compromise so as to keep the ground state as accurate as possible without sacrificing the excited state asymptotic behavior entirely. Luckily, the excited states are smooth for all ζ parameters (not shown here). The parameter set is the one-site model with $m\omega^2 = 0.003, g = 0.0075, e_{d_1} = 0.05, U = 0$ with 101 metal states evenly distributed with energy spacing $dE = \frac{\Gamma}{10}$ (i.e. the full band width is 10Γ).

In practice, picking the optimal ζ is usually a compromise between the criteria above: we expect that a large ζ would be best if we seek ground state accuracy while a smaller ζ would be best for achieving the correct excited state asymptotic behavior and smooth surfaces. This intuition is confirmed in Fig. 2. In Fig. 2(a), we plot the error in the energy of the ground state as a function of ζ. As we would guess, the larger ζ is, the less mixing there is

between S_0 and S_1, S_2, and therefore the more accurate S_0 is. Next, in Fig. 2(b), we plot the asymptotic energy difference between $E(S_2)$ (by DW-SA-cCASSCF(2,2)) and $E(ne = 0)$ (the diabatic state whose number of electrons on the impurity is 0) as a function of ζ. We see clearly that $E(S_2)$ is closer to $E(ne = 0)$ when ζ is small and there is more mixing between S_0 and S_1, S_2 during the orbital optimization. Lastly, as far as the smoothness is concerned, we find that surfaces are all smooth for $\zeta = 20, 30, 40, 50$ for the one-site $U = 0$ model.

From the considerations above, in order to maintain reasonable ground state accuracy while keeping the excited state asymptotic behavior as accurate as possible, we chose $\zeta = 40$ as a compromise value. (Note that for the two-site model, $\zeta = 10$ is a better compromise; See Section C). In short, our rule of thumb in picking the proper ζ is that we will need to sacrifice some ground-state energy accuracy in order to recover a smooth and qualitatively correct surface suitable for nonadiabatic dynamics.

C A Partially Localized Constraint Versus a Fully Localized Constraint For a Two-Site Hamiltonian With $U = 0.1$

Finally, in Figs. 3, 4 and 5, we plot results for two different constraints: partially localized constraint (denoted as "pc" , see Eqn. 39) v.s. fully localized constraint (denoted as "fc", see Eqn. 42). As one can see in Fig. 3(a), "fc" S_1 and S_2 energies are much larger than the corresponding "pc" energies for $\epsilon_d \in [-0.05, 0.19]$, and the former also have a large discontinuity around $\epsilon_d = 0.19$. At this discontinuity point, in Fig. 3(c), we can clearly see that the "fc" ground state energy recovers the RHF result. A similar anomaly is found in Fig. 4, where we plot the total number of electron on the impurity ($\langle n_{tot} \rangle$) against the exact numerical renormalization group (NRG). In Fig. 4(a), for "pc", two excited state populations have a transition around $\epsilon_d = -0.05$: from 3 to 1 for S_1 and from 4 to 0 for S_2. However, for "fc", S_1 and S_2 do not capture this population transition. Moreover, in Fig. 4(c), the fc S_0 population is wrong (and equal to the RHF answer) when $\langle n_{tot} \rangle$ changes from 2 to 0 around $\epsilon_d \in [0.1, 0.19]$; the fc results display a discontinuity at $\epsilon_d = 0.19$. Altogether

we may hypothesize that the fc method fails to describe how the active orbital switches locality around $\epsilon_d = -0.05$. This hypothesis is confirmed in Fig. 5(a), where we plot the impurity population on the pc and fc active orbitals. For the pc method, the HOMO is not always localized on the impurity (true for $\epsilon_d < -0.05$) and in fact becomes a bath orbital for $\epsilon_d > -0.05$; however, for fc, the HOMO is always on the impurity. Such a change in frontier orbital localization can also be identified by the small tip/dip in Fig. 5(b), where we plot the eigenvalues of the impurity projection operator, $\hat{P}_{imp} = 2(d_1^\dagger d_1 + d_2^\dagger d_2)$. All told, the pc approach appears to be a far more robust approach than does the fc approach. Note that, in the range $\epsilon_d \in [-0.3, -0.25]$ (in Fig. 4(b)) or $\epsilon_d \in [0.15, 0.2]$ (in Fig. 4(c)), UHF results become non-smooth whereas pc results remain smooth; this attribute is encouraging as far as the potential to run dynamics.

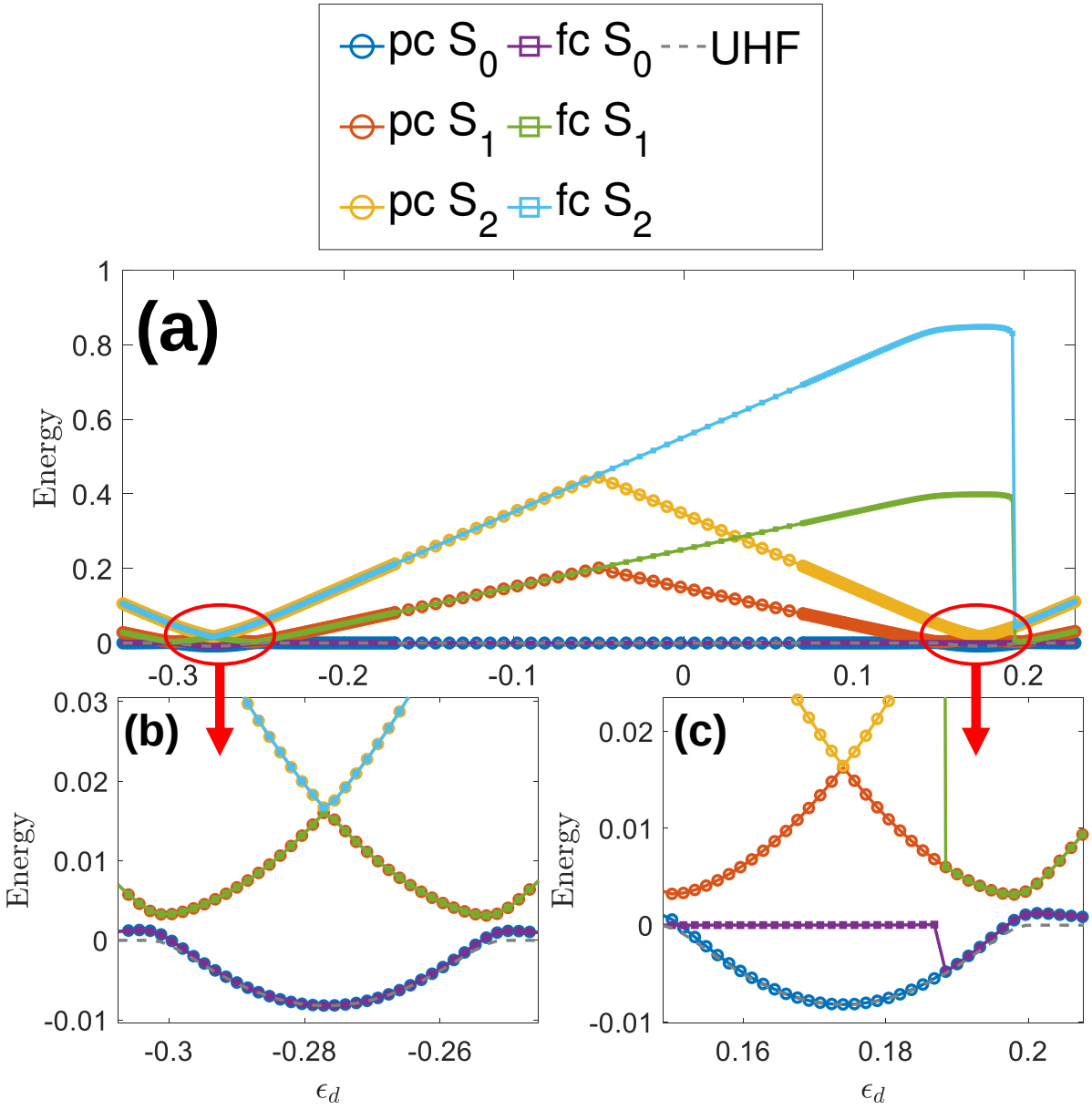

Figure 3: The partially constrained (pc) and fully constrained (fc) energies relative to RHF as a function of the onsite energy ϵ_d. (a) The full range of ϵ_d; (b) Zoom in on the left red circle in (a); (c) Zoom in on the right red circle in (a). Note that the fc energies are not smooth in Fig. (c) and the fc S_1, S_2 energies are far too large compared to pc for $\epsilon_d \in [-0.05, 0.19]$ in Fig. (a). The parameter set is= a two-site model with $\epsilon_d = \epsilon_{d_1} = \epsilon_{d_2}, \Gamma = 0.01, t_d = 0.2, U = 0.1, \zeta = 10$ and 31 metal states evenly distributed with energy spacing $dE = \frac{\Gamma}{10}$ (i.e. the full band width is 3Γ).

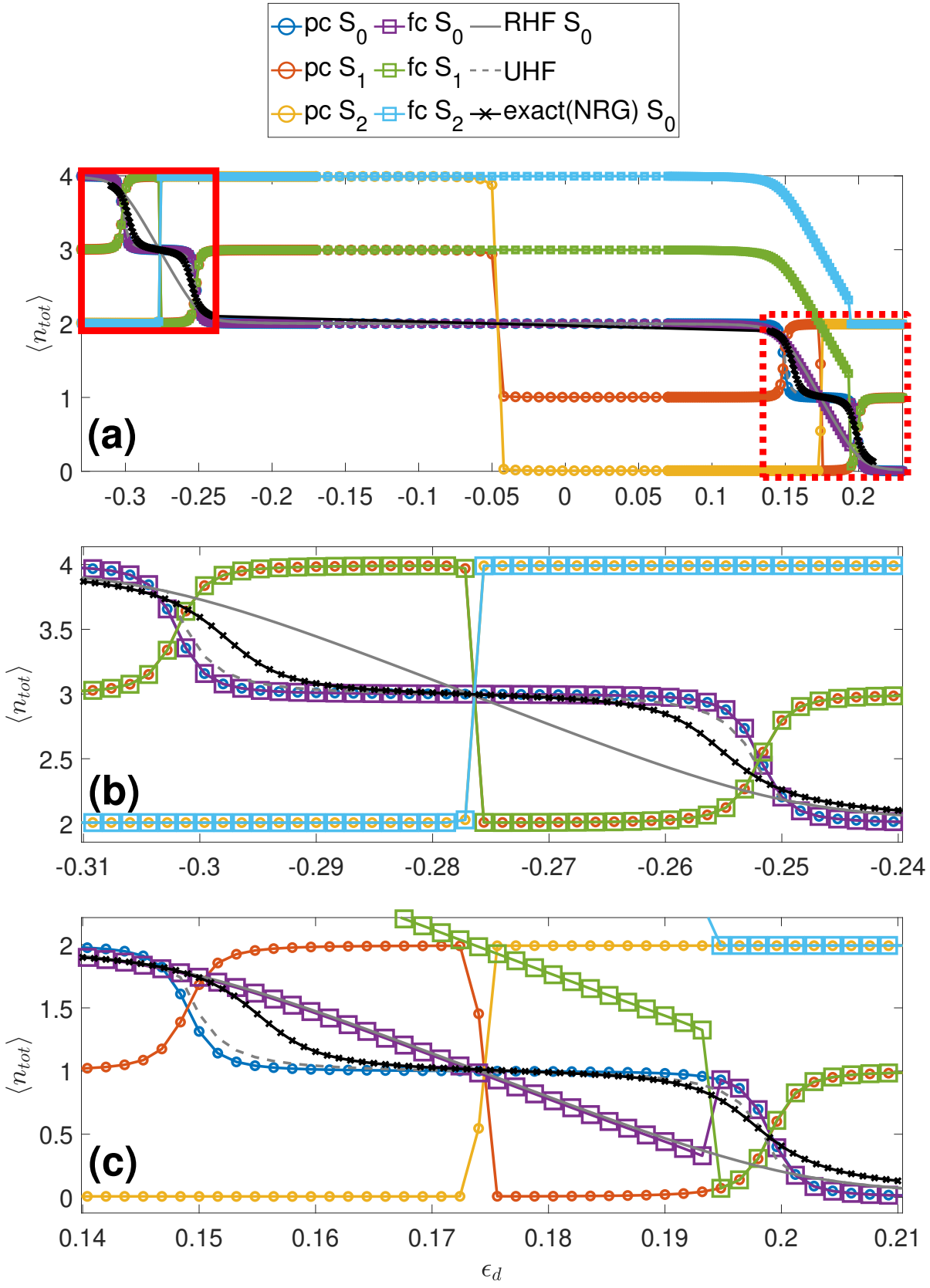

Figure 4: The pc and fc total number of electrons on the impurity as a function of the onsite energy ϵ_d. (a) The full range of ϵ_d; (b) Zoom in on the red solid box in (a); (c) Zoom in on the red dashed box in (a). The fc ground state is neither smooth nor accurate compared to the NRG ground state electron population in Fig. (c); the pc results are more accurate relatively and always smooth. The parameter set is the two-site model with $\epsilon_d = \epsilon_{d_1} = \epsilon_{d_2}, \Gamma = 0.01, t_d = 0.2, U = 0.1, \zeta = 10$ and 31 metal states evenly distributed with energy spacing $dE = \frac{\Gamma}{10}$ (i.e. the full band width is 3Γ).

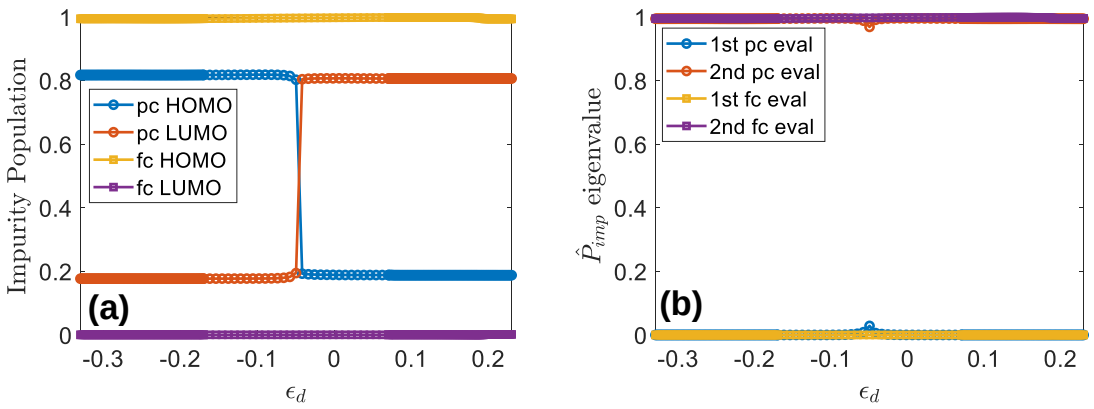

Figure 5: An analysis of the pc and fc active (or frontier) orbitals. (a) Impurity population. (b) The eigenvalues of the impurity projector $\hat{P}_{imp}$. Note that the HOMO/LUMO impurity populations switch at $\epsilon_d = -0.05$ only for pc (but not for fc) in Fig. (a), leading to the tip/dip in the eigenvalue curve in Fig. (b). This switch enables smooth curves over the full range of ϵ_d as shown in Figs. 3 and 4. The parameter set is the two-site model with $\epsilon_d = \epsilon_{d_1} = \epsilon_{d_2}, \Gamma = 0.01, t_d = 0.2, U = 0.1, \zeta = 10$ and 31 metal states evenly distributed with energy spacing $dE = \frac{\Gamma}{10}$ (i.e. the full band width is 3Γ).

Lastly, in Fig. 6, we investigate how these different constraints behave as a function of the dynamical weighting parameter ζ. In particular, we plot the ground and excited energy (relative to RHF) of fc and pc for a dynamical weighting parameter $\zeta = 10, 20, 30, 40$. One can see that the fc excited state energies S_1 and S_2 never recognize a curve crossing around $\epsilon_d = -0.05$ which eventually leads to a discontiuity; the pc excited states do recognize a curve crossing but only when $\zeta = 10, 20$. Altogether, the fc constraint would appear inferior to the pc constraint.

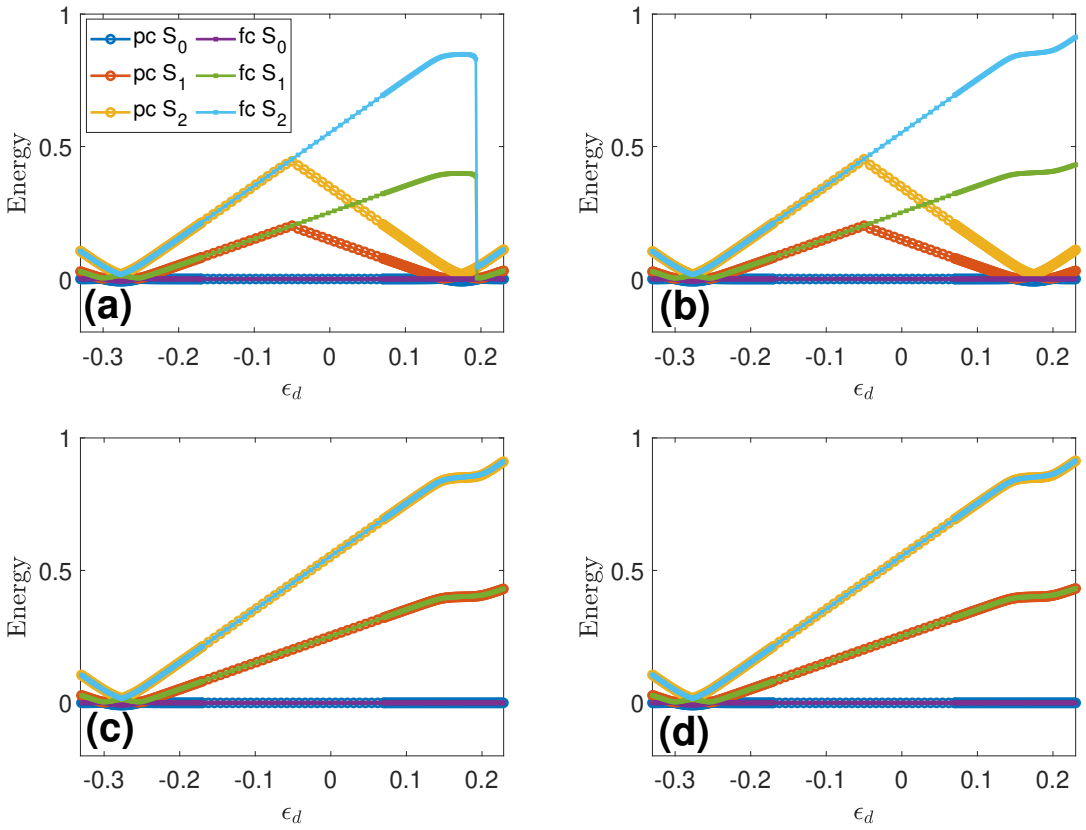

Figure 6: Sensitivity of the pc and fc excited state energies as a function of the dynamical weighting parameter ζ. (a) $\zeta = 10$; (b) $\zeta = 20$; (c) $\zeta = 30$; (3) $\zeta = 40$. Note that the pc approach recognizes a curve crossing around $\epsilon_d = -0.05$ for $\zeta = 10, 20$ (though $\zeta = 30, 40$ does not). This switch enables smooth curves over the full range of ϵ_d as shown in Figs. 3 and 4. The parameter set is the two-site model $\epsilon_d = \epsilon_{d_1} = \epsilon_{d_2}, \Gamma = 0.01, t_d = 0.2, U = 0.1$ with 31 evenly distributed metal states with energy spacing $dE = \frac{\Gamma}{10}$ (i.e. the full band width is 3Γ).

V Discussion

So far, we have demonstrated that cCASSCF potential energy surfaces should be useful for modeling electron transfer processes at surfaces. That being said, in order to apply them in practice, two more practical quantities must be extracted. First, if we seek to run fully nonadiabatic dynamics in the spirit of an FSSH-ER algorithm,[31] we will require system-bath couplings that capture non-vibrational electronic relaxation. Second, if we seek to extract Marcus-like rate expression, we will need diabatic curves and diabatic couplings. We will now show how these quantities can be obtained.

A System-Bath Couplings

In order to describe the molecule-metal coupling in a charge transfer process using as few singly-excitation configurations as possible (for reasons of efficiency), we will consider only single excitations between core and active ($i \rightarrow t, u$) as well as single excitations between active and virtual ($t, u \rightarrow a$).

Let us denote our three DW-SA-cCASSCF(2,2) system CI states as $\{|\Psi_0\rangle, |\Psi_1\rangle, |\Psi_2\rangle\}$:

$$\Omega_S \equiv \{|\Psi_0\rangle, |\Psi_1\rangle, |\Psi_2\rangle\} \tag{58}$$

following the conventions of Eq. 44 above. For the three system CI states above, we focus on those bath states that arise from single excitations with reference to three configurations: $|t\bar{t}\rangle$, $|u\bar{u}\rangle$ and $|t\bar{u} + u\bar{t}\rangle$. In general, identifying and indexing excitations from a multireference configuration can be very difficult and tedious. Howevever, for CASSCF(2,2) refrence, this task is not terrible. If we define the reference state configuration to be $|t\bar{t}\rangle$, then there are four relevant classes of excited state slater determinants composed of molecular orbitals i, t, u, a:

$$\begin{aligned} |\Psi_i^u\rangle &= |\cdots u\bar{i} \cdots t\bar{t}\rangle \\ |\Psi_t^a\rangle &= |\cdots i\bar{i} \cdots a\bar{t}\rangle \\ |\Psi_{i\bar{t}}^{u\bar{u}}\rangle &= |\cdots u\bar{i} \cdots t\bar{u}\rangle \\ |\Psi_{t\bar{t}}^{a\bar{u}}\rangle &= |\cdots i\bar{i} \cdots a\bar{u}\rangle \end{aligned} \tag{59}$$

Therefore, let us denote our bath CI states as:

$$\Omega_B \equiv \{|\Psi_i^u\rangle, |\Psi_t^a\rangle, |\Psi_{i\bar{t}}^{u\bar{u}}\rangle, |\Psi_{t\bar{t}}^{a\bar{u}}\rangle\} \tag{60}$$

Having defined the system and the bath states, the Hamiltonian for the whole universe can be schematically represented as:

$$
\begin{aligned}
H &= \left[\begin{array}{c|c} \textbf{system} & \textbf{coupling} \\ \hline \textbf{coupling} & \textbf{bath} \end{array}\right] \\
\textbf{system} &= \begin{bmatrix} \langle\Psi_0|H|\Psi_0\rangle & 0 & 0 \\ 0 & \langle\Psi_1|H|\Psi_1\rangle & 0 \\ 0 & 0 & \langle\Psi_2|H|\Psi_2\rangle \end{bmatrix} \\
\textbf{coupling} &= \begin{bmatrix} \langle\Psi_0|H|S_i^u\rangle & \langle\Psi_0|H|S_t^a\rangle & \langle\Psi_0|H|S_{i\bar{t}}^{u\bar{u}}\rangle & \langle\Psi_0|H|S_{t\bar{t}}^{a\bar{u}}\rangle \\ \langle\Psi_1|H|S_i^u\rangle & \langle\Psi_1|H|S_t^a\rangle & \langle\Psi_1|H|S_{i\bar{t}}^{u\bar{u}}\rangle & \langle\Psi_1|H|S_{t\bar{t}}^{a\bar{u}}\rangle \\ \langle\Psi_2|H|S_i^u\rangle & \langle\Psi_2|H|S_t^a\rangle & \langle\Psi_2|H|S_{i\bar{t}}^{u\bar{u}}\rangle & \langle\Psi_2|H|S_{t\bar{t}}^{a\bar{u}}\rangle \end{bmatrix} \\
\textbf{bath} &= \begin{bmatrix} \langle S_i^u|H|S_i^u\rangle & * & * & * \\ * & \langle S_t^a|H|S_t^a\rangle & * & * \\ * & * & \langle S_{i\bar{t}}^{u\bar{u}}|H|S_{i\bar{t}}^{u\bar{u}}\rangle & * \\ * & * & * & \langle S_{t\bar{t}}^{a\bar{u}}|H|S_{t\bar{t}}^{a\bar{u}}\rangle \end{bmatrix}
\end{aligned}
\tag{61}
$$

Here, we have employed spin-adapted singlet configurations:

$$
\begin{aligned}
|S_i^u\rangle &= \frac{|\Psi_i^u\rangle + |\Psi_{\bar{i}}^{\bar{u}}\rangle}{\sqrt{2}} \\
|S_t^a\rangle &= \frac{|\Psi_t^a\rangle + |\Psi_{\bar{t}}^{\bar{a}}\rangle}{\sqrt{2}} \\
|S_{i\bar{t}}^{u\bar{u}}\rangle &= \frac{|\Psi_{i\bar{t}}^{u\bar{u}}\rangle + |\Psi_{t\bar{i}}^{u\bar{u}}\rangle}{\sqrt{2}} \\
|S_{t\bar{t}}^{a\bar{u}}\rangle &= \frac{|\Psi_{t\bar{t}}^{a\bar{u}}\rangle + |\Psi_{t\bar{t}}^{u\bar{a}}\rangle}{\sqrt{2}}
\end{aligned}
\tag{62}
$$

We may then construct *many-body* hybridization function between the system excited states and the bath (which is analogous to the single-orbital hybridization in Eq. 35):

$$
\begin{aligned}
\tilde{\Gamma}_1 &= 2\pi \sum_B |\langle\Psi_B|H|\Psi_1\rangle|^2 \delta(E_B - E_1) \\
\tilde{\Gamma}_2 &= 2\pi \sum_B |\langle\Psi_B|H|\Psi_2\rangle|^2 \delta(E_B - E_2),
\end{aligned}
\tag{63}
$$

where $|\Psi_B\rangle$ is the *bath* state defined in Eq. 60 and E_B is the *bath* state energy. $|\Psi_1\rangle, |\Psi_2\rangle$ are two excited *system* states defined in Eq. 58 and E_1, E_2 are excited *system* state energies.

Consider the $U = 0$ case. In Fig. 7, we plot the first and the second excited state hybridizations, $\tilde{\Gamma}_1$ and $\tilde{\Gamma}_2$, respectively. The magnitudes of both $\tilde{\Gamma}_1$ and $\tilde{\Gamma}_2$ are of the same order as the impurity-bath hybridization Γ as found in Ref. 31. More interestingly, in both cases, there is a dip in the effective hybridization around $\epsilon_d(x) = 0$. For the $\tilde{\Gamma}_1$ case, this interesting behavior was reported previously in Ref. 31. In Ref. 31, it was argued that this dip arises from the fact that although electronic relaxation between molecule and metal is dictated by the hybridization far away from the crossing, near the crossing the relaxation is dictated by vibronic or electron-phonon interactions (which leads to the dip at $\epsilon_d(x) = 0$). To better understand the origin of this effect, in Fig. 8(b), we plot the density of bath states for the case $\Gamma = 0.01$. We find that the density of states is roughly constant for the $S_0 - S_1$ crossing as a function of $\epsilon_d(x)$. Thus, at least in one case, this dip is indeed caused by the changing character of the electronic states around the crossing point. As a practical matter, we note size of this dip does depend on the extent of dynamical weighting (not shown); at the same time however, following the results in Ref. 31, we do not expect this dip to have a major dynamical impact.

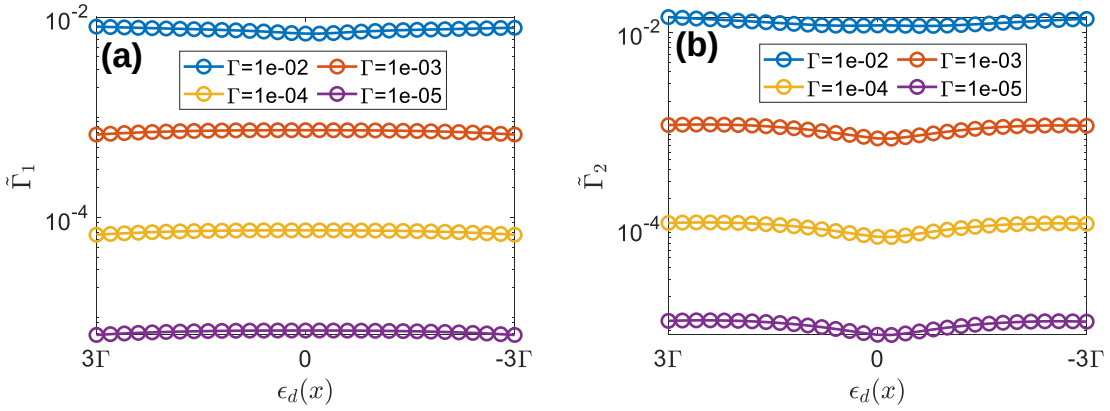

Figure 7: The hybridization between a DW-SA-pcCASSCF(2,2) ($\zeta = 40$) excited state and the bath states. (a) The hybridization for state S_1 ($\tilde{\Gamma}_1$); (b) the hybridization for state S_2 ($\tilde{\Gamma}_2$). We investigate four different Γs: $10^{-2}, 10^{-3}, 10^{-4}, 10^{-5}$. Note that both $\tilde{\Gamma}_1$ and $\tilde{\Gamma}_2$ have a dip at the symmetric point, where the onsite energy $\epsilon_d(x)$ reaches the fermi level $\epsilon_f = 0$. We calculate $\tilde{\Gamma}_1$ and $\tilde{\Gamma}_2$ using a lorentzian function to approximate the delta function in Eq. 63: i.e. $\delta(x - x_0) \approx \frac{1}{\pi} \frac{\sigma/2}{(x-x_0)^2+(\sigma/2)^2}$ with the full width at half maximum (FWHM) $\sigma = \Gamma$. The parameter set is theone-site model with $m\omega^2 = 0.003, g = 0.0075, e_{d_1} = 0.05, U = 0$ with 101 evenly distributed metal states with energy spacing $dE = \frac{\Gamma}{10}$ (i.e. the full band width is 10Γ).

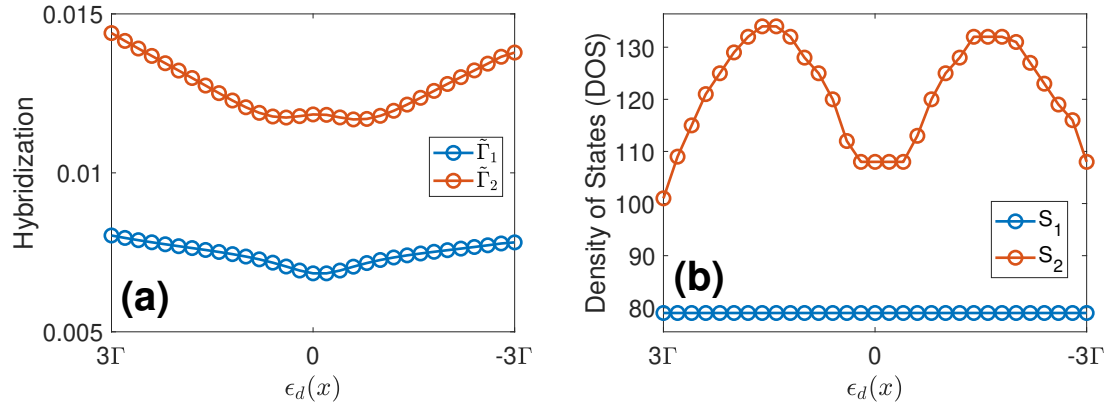

Figure 8: (a) The many-body hybridizations $\tilde{\Gamma}_1$ and $\tilde{\Gamma}_2$; (b) The density of states (DOS) around the S_1 and S_2 energy levels. Note that the DOS around S_1 is effectively constant so that the dip in $\tilde{\Gamma}_1$ at $\epsilon_d = 0$ is caused exclusively by the change in electronic wavefunctions at the crossing point. The case of S_2 is slightly more difficult to interpret, but the fact that the DOS seems to have two maxima whereas the hybridization $\tilde{\Gamma}_2$ has two minima would also suggest that the variations in $\tilde{\Gamma}_2$ are not due to DOS effects. Here, the DOS(S_1) is calculated by counting in those bath states whose energy is within the energy window $[E(S_1) - \Gamma/2, E(S_1) + \Gamma/2]$ (same for DOS(S_2)). The parameter set is the one-site model with $m\omega^2 = 0.003, g = 0.0075, e_{d_1} = 0.0365, \Gamma = 0.01, U = 0, \zeta = 40$ with 101 evenly distributed metal states with energy spacing $dE = \frac{\Gamma}{10}$ (i.e. the full band width is 10Γ).

B Diabatization

For the purposes of modeling electron transfer with Marcus theory,[16] it can be very helpful to work with a set of diabatic states. Luckily, for a CASSCF(2,2) calculation, generating such diabatic states is often straightforward. Here, we will generate an adiabatic-to-diabatic transformation by diagonalizing the impurity projector $\hat{w}$ in the basis of the three DW-SA-cCASSCF(2,2) states (S_0, S_1 and S_2). For the one-impurity Hamiltonian in Eq. 34, we diagonalize $\hat{w} = d^\dagger d$:

$$C_{diab}^\dagger \hat{w} C_{diab} = n_{diab} \tag{64}$$

The transformed diabatic Hamiltonian is then:

$$H_{diab} = C_{diab}^\dagger \hat{H} C_{diab} \tag{65}$$

In Fig. 9, we plot the extracted diabatic energies for the one-site Hamiltonian in Eq. 34. From the data, it is clear that the resulting energies and couplings are smooth: the diabatization is robust.

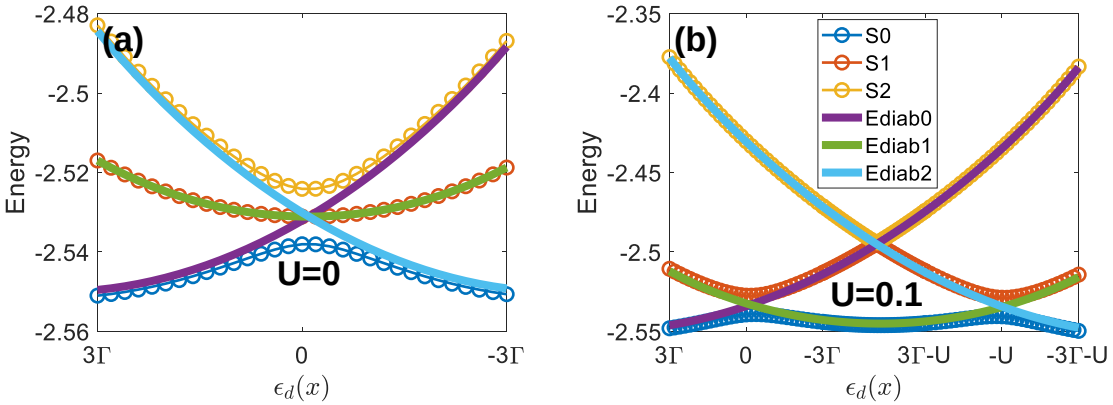

Figure 9: The adiabatic and diabatic energies as a function of $\epsilon_d(x)$, for (a) $U = 0$; (b) $U = 0.1$. The diabatization uses the three DW-SA-pcCASSCF(2,2) ($\zeta = 40$) states as the adiabatic state basis. The parameter set is the one-site model and for $U = 0$, we set $m\omega^2 = 0.003, g = 0.0075, e_{d_1} = 0.0365, \Gamma = 0.01$. For $U = 0.1$, we set $m\omega^2 = 0.001, g = 0.0075, e_{d_1} = 0.06, \Gamma = 0.01$. There are 101 metal states evenly distributed with energy spacing $dE = \frac{\Gamma}{10}$ (i.e. the full band width is 10Γ).

Next, in Fig. 10, we plot the diabatic couplings between the diabat 0 and the diabat 1

(V_{01}) as a function of ϵ_d and for a range of different Γs: $10^{-2}, 10^{-3}, 10^{-4}, 10^{-5}$. We investigate both the $U = 0$ and $U = 0.1$ cases. Note that these couplings are nearly identical across all values of ϵ_d and both values of U; the couplings depend more than anything on the value of Γ. Note that the values of $|V_{01}|$ are identical (up to 10^{-15} significant digits) with the values of $|V_{12}|$. The diabatic coupling between the diabat 0 and the diabat 2 (V_{02}) is effectively zero (not shown).

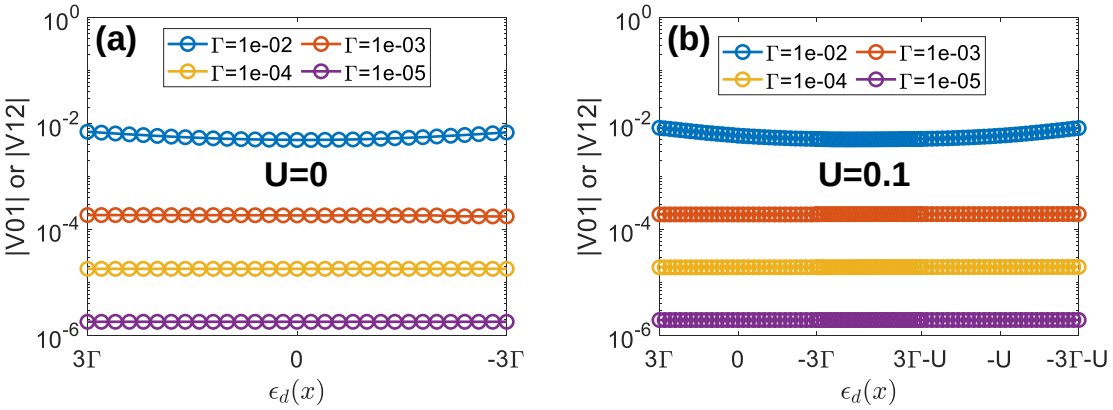

Figure 10: The diabatic coupling $|V_{01}|$ (which is numerically found to be equal to $|V_{12}|$) as a function of $\epsilon_d(x)$, for (a) $U = 0$; (b) $U = 0.1$, for four different Γs: $10^{-2}, 10^{-3}, 10^{-4}, 10^{-5}$. Note that diabat 0 and diabat 2 are indirectly coupled with each other according to V_{01} and V_{12} but the direct coupling V_{02} is 0. The diabatization uses the three DW-SA-pcCASSCF(2,2) ($\zeta = 40$) states as the adiabatic state basis. The parameter set is $U = 0$, $m\omega^2 = 0.003, g = 0.0075, e_{d_1} = 0.05$ or $U = 0.1$, $m\omega^2 = 0.001, g = 0.0075, e_{d_1} = 0.06$. We include 101 metal states evenly distributed with energy spacing $dE = \frac{\Gamma}{10}$ (i.e. the full band width is 10Γ).

Lastly, in Fig. 11, we plot the diabatic coupling V_{01}, as well as the adiabatic $S_0 - S_1$ minimum excitation gap, as a function of the molecule-metal coupling Γ. We plot results with dynamically-weighted state-averaging (DW-SA, blue) and without any state-averaging (red). Several conclusions are apparent. First, the relationship between $V_{01} - \Gamma$ and gap$-\Gamma$ are almost linear; see the dashed line for linear fits. Note that a linear relationship between the gap and Γ was found previously in Ref. 31), where it was shown that a reduced model Hamiltonian can in fact recover Marcus's electrochemical rate expression for the case $U = 0$. Second, one finds that DW-SA reduces both the gap and the diabatic coupling (compared to no DW-SA); this finding is perhaps expected because, in the gas phase, without state

averaging, one does not properly the ground state and the excited state (and the gap is often too large). Third, by comparing (a) with (b) or (c) with (d), we find that the results do not change a lot after adding electron-electron repulsion ($U = 0.1$); it would seem that, within this model, the main impact of electron-electron repulsion is on the barriers present in the ground state. For instance, for the $U = 0$ case in Fig. 9(a), the symmetric barrier is 0.013; for the $U = 0.1$ case in Fig. 9(b), the symmetric barrier is 0.007 for the middle well and 0.009 for the left/right well. Fourth, if one looks carefully at the $\zeta = 40$ lines, one can discern a slight uphill behavior for large (around $\Gamma = 0.01$); this feature arises because the weight of the ground state S_0 increases as the gap grows; after all, ζ is a constant. In the future, one may want to employ a ζ that depends on Γ; in practice, this would mean choosing weighting parameters depending on the distance from the molecule to the metal.

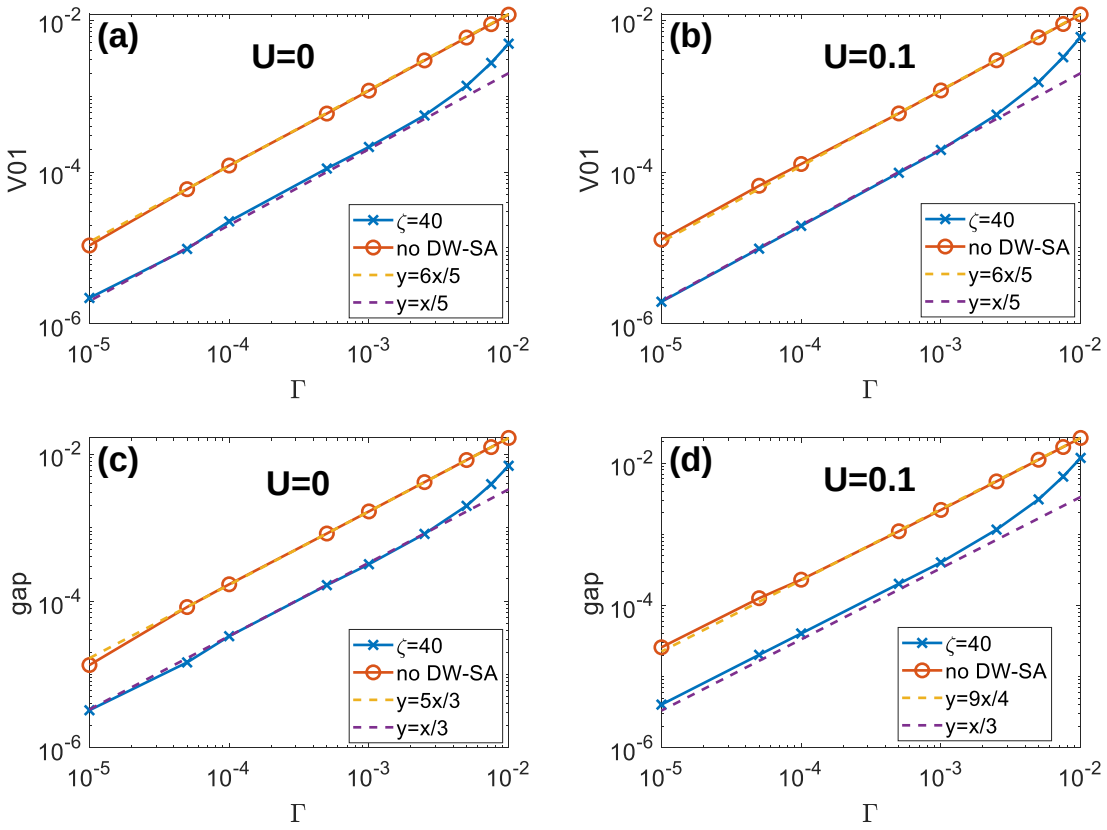

Figure 11: The diabatic coupling $|V_{01}|$ (the same as $|V_{12}|$) at the minimum crossing, for (a) $U = 0$; (b) $U = 0.1$. The $S_0 - S_1$ excitation gap at the minimum crossing, for (c) $U = 0$; (d) $U = 0.1$. Note that both quantities effectively depend linearly on the system-bath coupling Γ. Also note that the slight uphill behavior for the $\zeta = 40$ line arises because the weight on the ground state S_0 increases for large ζ. The parameter set is the one-site model with $U = 0$, $m\omega^2 = 0.003, g = 0.0075, e_{d_1} = 0.05$ or with $U = 0.1$, $m\omega^2 = 0.001, g = 0.0075, e_{d_1} = 0.06$. We include 101 metal states evenly distributed with energy spacing $dE = \frac{\Gamma}{10}$ (i.e. the full band width is 10Γ).

VI Conclusions

In this paper, we have investigated a novel dynamically-weighted state-averaged constrained CASSCF(2,2) (DW-SA-cCASSCF(2,2)) electronic structure approach for studying open quantum systems and in particular molecules on metal surfaces. We have focused on this approach after several aborted attempts with other methods. For several reasons, the present method seems to be an excellent candidate for future work navigating electron transfer at a metal surface: (i) The adiabatic energies are smooth as a result of state-averaging and implementing a constraint that forces the active space to overlap with the impurity; (ii) Diabatization is possible and Marcus curves can be generated; (iii) The approach overlaps well with standard CASSCF theory and we can employ (with modification) many standard quantum chemistry tools to solve the necessary equations. In the end, although DW-SA-cCASSCF(2,2) wavefunctions are slightly more involved than standard multireference approaches, the active space is small and convergence can be achieved.

Looking forward, the present method should be applicable to realistic, *ab initio* systems, which we will report in a future publication. We also anticipate running fewest switches surface hopping (FSSH) calculations in the future where we will studying molecules moving (adiabatically or nonadiabatically) along metal surfaces once a gradient[53] has been constructed; obviously, studying electrochemical dynamics will be easier than studying photoelectrochemical dynamics. Finally, in this paper, by working with a model Hamiltonian, we have ignored the question of electron-electron exchange that inevitably complicates any description of a metal (where Hartree-Fock exchange is not physical). In the future, when working with realistic (fully ab initio) models of molecules on surfaces, it would be very helpful if we can merge the present CASSCF(2,2) wavefunction calculation with a DFT framework, either in the spirit of multiconfiguration pair-density functional theory (MC-PDFT),[54] time-dependent density functional theory plus one double (TDDFT-1D),[55] or hole–hole Tamm–Dancoff approximated (hh-TDA).[56] Armed with such an algorithm, one anticipates many new calculations that one would like to tackle at a catalytic metal surface.

Acknowledgement

This work was supported by the U.S. Air Force Office of Scientific Research (USAFOSR) under Grant Nos. FA9550-18-1-0497 and FA9550-18-1-0420. We thank the DoD High Performance Computing Modernization Program for computer time. We also thank Xinchun Wu for making corrections to the original draft.

VII Appendix

A Single Excitation Matrix Elements

In this subsection, for the sake of concreteness, we report the matrix element between the system states (defined in Eq. 58) and the bath states (defined in Eq. 60).

$$\begin{aligned}\langle t\bar{t}|H|S_i^u\rangle &= (\langle\cdots i\bar{i}\cdots t\bar{t}|H|\cdots u\bar{i}\cdots t\bar{t}\rangle + \langle\cdots i\bar{i}\cdots t\bar{t}|H|\cdots i\bar{u}\cdots t\bar{t}\rangle)/\sqrt{2}\\ &= \sqrt{2}*(F_{iu}^I + 2(iu|tt) - (it|tu))\end{aligned} \tag{66}$$

$$\begin{aligned}\langle t\bar{t}|H|S_t^a\rangle &= (\langle\cdots i\bar{i}\cdots t\bar{t}|H|\cdots i\bar{i}\cdots a\bar{t}\rangle + \langle\cdots i\bar{i}\cdots t\bar{t}|H|\cdots i\bar{i}\cdots t\bar{a}\rangle)/\sqrt{2}\\ &= \sqrt{2}*(F_{ta}^I + (ta|\bar{t}\bar{t}))\end{aligned} \tag{67}$$

$$\begin{aligned}\langle t\bar{t}|H|S_{i\bar{t}}^{u\bar{u}}\rangle &= (\langle\cdots i\bar{i}\cdots t\bar{t}|H|\cdots u\bar{i}\cdots t\bar{u}\rangle + \langle\cdots i\bar{i}\cdots t\bar{t}|H|\cdots u\bar{t}\cdots i\bar{u}\rangle)/\sqrt{2}\\ &= \sqrt{2}*(iu|\bar{t}\bar{u})\end{aligned} \tag{68}$$

$$\begin{aligned}\langle t\bar{t}|H|S_{t\bar{t}}^{a\bar{u}}\rangle &= (\langle\cdots i\bar{i}\cdots t\bar{t}|H|\cdots i\bar{i}\cdots a\bar{u}\rangle + \langle\cdots i\bar{i}\cdots t\bar{t}|H|\cdots i\bar{i}\cdots u\bar{a}\rangle)/\sqrt{2}\\ &= \sqrt{2}*(ta|\bar{t}\bar{u})\end{aligned} \tag{69}$$

$$\begin{aligned}\langle u\bar{u}|H|S_i^u\rangle &= (\langle\cdots i\bar{i}\cdots u\bar{u}|H|\cdots u\bar{i}\cdots t\bar{t}\rangle + \langle\cdots i\bar{i}\cdots u\bar{u}|H|\cdots i\bar{u}\cdots t\bar{t}\rangle)/\sqrt{2}\\ &= -\sqrt{2}*(it|\bar{u}\bar{t})\end{aligned} \tag{70}$$

$$\begin{aligned}\langle u\bar{u}|H|S_t^a\rangle &= (\langle\cdots i\bar{i}\cdots u\bar{u}|H|\cdots i\bar{i}\cdots a\bar{t}\rangle + \langle\cdots i\bar{i}\cdots u\bar{u}|H|\cdots i\bar{i}\cdots t\bar{a}\rangle)/\sqrt{2} \\ &= \sqrt{2} * (ua|\bar{u}\bar{t})\end{aligned} \tag{71}$$

$$\begin{aligned}\langle u\bar{u}|H|S_{i\bar{t}}^{u\bar{u}}\rangle &= (\langle\cdots i\bar{i}\cdots u\bar{u}|H|\cdots u\bar{i}\cdots t\bar{u}\rangle + \langle\cdots i\bar{i}\cdots u\bar{u}|H|\cdots u\bar{t}\cdots i\bar{u}\rangle)/\sqrt{2} \\ &= -\sqrt{2} * (F_{it}^I + 2(it|uu) - (iu|ut))\end{aligned} \tag{72}$$

$$\begin{aligned}\langle u\bar{u}|H|S_{t\bar{t}}^{a\bar{u}}\rangle &= (\langle\cdots i\bar{i}\cdots u\bar{u}|H|\cdots i\bar{i}\cdots a\bar{u}\rangle + \langle\cdots i\bar{i}\cdots u\bar{u}|H|\cdots i\bar{i}\cdots u\bar{a}\rangle)/\sqrt{2} \\ &= \sqrt{2} * (F_{ua}^I + (ua|\bar{u}\bar{u}))\end{aligned} \tag{73}$$

$$\begin{aligned}\langle u\bar{t}|H|S_i^u\rangle &= (\langle\cdots i\bar{i}\cdots u\bar{t}|H|\cdots u\bar{i}\cdots t\bar{t}\rangle + \langle\cdots i\bar{i}\cdots u\bar{t}|H|\cdots i\bar{u}\cdots t\bar{t}\rangle)/\sqrt{2} \\ &= \sqrt{2} * (-F_{it}^I - (it|\bar{t}\bar{t}))\end{aligned} \tag{74}$$

$$\begin{aligned}\langle u\bar{t}|H|S_t^a\rangle &= (\langle\cdots i\bar{i}\cdots u\bar{t}|H|\cdots i\bar{i}\cdots a\bar{t}\rangle + \langle\cdots i\bar{i}\cdots u\bar{t}|H|\cdots i\bar{i}\cdots t\bar{a}\rangle)/\sqrt{2} \\ &= \sqrt{2} * (F_{ua}^I + (ua|\bar{t}\bar{t}))\end{aligned} \tag{75}$$

$$\begin{aligned}\langle u\bar{t}|H|S_{i\bar{t}}^{u\bar{u}}\rangle &= (\langle\cdots i\bar{i}\cdots u\bar{t}|H|\cdots u\bar{i}\cdots t\bar{u}\rangle + \langle\cdots i\bar{i}\cdots u\bar{t}|H|\cdots u\bar{t}\cdots i\bar{u}\rangle)/\sqrt{2} \\ &= -\sqrt{2} * (it|\bar{t}\bar{u})\end{aligned} \tag{76}$$

$$\begin{aligned}\langle u\bar{t}|H|S_{t\bar{t}}^{a\bar{u}}\rangle &= (\langle\cdots i\bar{i}\cdots u\bar{t}|H|\cdots i\bar{i}\cdots a\bar{u}\rangle + \langle\cdots i\bar{i}\cdots u\bar{t}|H|\cdots i\bar{i}\cdots u\bar{a}\rangle)/\sqrt{2} \\ &= \sqrt{2} * (ua|\bar{t}\bar{u})\end{aligned} \tag{77}$$

$$\begin{aligned}\langle t\bar{u}|H|S_i^u\rangle &= (\langle\cdots i\bar{i}\cdots t\bar{u}|H|\cdots u\bar{i}\cdots t\bar{t}\rangle + \langle\cdots i\bar{i}\cdots t\bar{u}|H|\cdots i\bar{u}\cdots t\bar{t}\rangle)/\sqrt{2} \\ &= \sqrt{2}((iu|\bar{u}\bar{t})\end{aligned} \tag{78}$$

$$\begin{aligned}\langle t\bar{u}|H|S_t^a\rangle &= (\langle\cdots i\bar{i}\cdots t\bar{u}|H|\cdots i\bar{i}\cdots a\bar{t}\rangle + \langle\cdots i\bar{i}\cdots t\bar{u}|H|\cdots i\bar{i}\cdots t\bar{a}\rangle)/\sqrt{2} \\ &= \sqrt{2} * (ta|\bar{u}\bar{t})\end{aligned} \tag{79}$$

$$\begin{aligned}\langle t\bar{u}|H|S_{i\bar{t}}^{u\bar{u}}\rangle &= (\langle\cdots i\bar{i}\cdots t\bar{u}|H|\cdots u\bar{i}\cdots t\bar{u}\rangle + \langle\cdots i\bar{i}\cdots t\bar{u}|H|\cdots u\bar{t}\cdots i\bar{u}\rangle)/\sqrt{2} \\ &= \sqrt{2} * (F_{iu}^I + (iu|\bar{u}\bar{u}))\end{aligned} \tag{80}$$

$$\begin{aligned}\langle t\bar{u}|H|S^{a\bar{u}}_{t\bar{t}}\rangle &= (\,\langle\cdots i\bar{i}\cdots t\bar{u}|H|\cdots i\bar{i}\cdots a\bar{u}\rangle + \langle\cdots i\bar{i}\cdots t\bar{u}|H|\cdots i\bar{i}\cdots u\bar{a}\rangle)/\sqrt{2} \\ &= \sqrt{2} * (F^I_{ta} + (ta|\bar{u}\bar{u}))\end{aligned} \tag{81}$$

Finally, again for completeness, let us now also report the diagonal matrix elements for the Hamiltonian in the basis of single excitation configurations:

$$\begin{aligned}\langle S^u_i|H|S^u_i\rangle &= \langle\cdots u\bar{i}\cdots t\bar{t}|H|\cdots u\bar{i}\cdots t\bar{t}\rangle + \langle\cdots u\bar{i}\cdots t\bar{t}|H|\cdots i\bar{u}\cdots t\bar{t}\rangle \\ &= E_{tt} + F^I_{uu} - F^I_{ii} + [2(uu|tt) - (ut|tu)] - [2(ii|tt) - (it|ti)] - (uu|ii) + 2(ui|iu)\end{aligned} \tag{82}$$

$$\begin{aligned}\langle S^a_t|H|S^a_t\rangle &= \langle\cdots i\bar{i}\cdots a\bar{t}|H|\cdots i\bar{i}\cdots a\bar{t}\rangle + \langle\cdots i\bar{i}\cdots a\bar{t}|H|\cdots i\bar{i}\cdots t\bar{a}\rangle \\ &= E_{tt} + F^I_{aa} - F^I_{tt} + [2(aa|tt) - (at|ta)] - [2(tt|tt) - (tt|tt)] - (aa|tt) + 2(at|ta)\end{aligned} \tag{83}$$

$$\begin{aligned}\langle S^{u\bar{u}}_{i\bar{t}}|H|S^{u\bar{u}}_{i\bar{t}}\rangle &= \langle\cdots u\bar{i}\cdots t\bar{u}|H|\cdots u\bar{i}\cdots t\bar{u}\rangle + \langle\cdots u\bar{i}\cdots t\bar{u}|H|\cdots u\bar{t}\cdots i\bar{u}\rangle \\ &= E_{uu} + F^I_{tt} - F^I_{ii} + [2(tt|uu) - (tu|ut)] - [2(ii|uu) - (iu|ui)] - (tt|ii) + 2(ti|it)\end{aligned} \tag{84}$$

$$\begin{aligned}\langle S^{a\bar{u}}_{t\bar{t}}|H|S^{a\bar{u}}_{t\bar{t}}\rangle &= \langle\cdots i\bar{i}\cdots a\bar{u}|H|\cdots i\bar{i}\cdots a\bar{u}\rangle + \langle\cdots i\bar{i}\cdots a\bar{u}|H|\cdots i\bar{i}\cdots u\bar{a}\rangle \\ &= E_{uu} + F^I_{aa} - F^I_{uu} + [2(aa|uu) - (au|ua)] - [2(uu|uu) - (uu|uu)] - (aa|uu) + 2(au|ua).\end{aligned} \tag{85}$$

Here E_{tt} and E_{uu} are the energies of the reference states:

$$E_{tt} = \langle\cdots i\bar{i}\cdots t\bar{t}|H|\cdots i\bar{i}\cdots t\bar{t}\rangle \tag{86}$$

$$E_{uu} = \langle\cdots i\bar{i}\cdots u\bar{u}|H|\cdots i\bar{i}\cdots u\bar{u}\rangle \tag{87}$$

References

(1) Waldeck, D.; Alivisatos, A.; Harris, C. Nonradiative damping of molecular electronic excited states by metal surfaces. *Surface Science* **1985**, *158*, 103–125.

(2) Wodtke*, A. M.; Tully, J. C.; Auerbach, D. J. Electronically non-adiabatic interactions of molecules at metal surfaces: Can we trust the Born–Oppenheimer approximation for surface chemistry? *International Reviews in Physical Chemistry* **2004**, *23*, 513–539.

(3) Bartels, C.; Cooper, R.; Auerbach, D. J.; Wodtke, A. M. Energy transfer at metal surfaces: the need to go beyond the electronic friction picture. *Chemical Science* **2011**, *2*, 1647–1655.

(4) Kandratsenka, A.; Jiang, H.; Dorenkamp, Y.; Janke, S. M.; Kammler, M.; Wodtke, A. M.; Bünermann, O. Unified description of H-atom–induced chemicurrents and inelastic scattering. *Proceedings of the National Academy of Sciences* **2018**, *115*, 680–684.

(5) Shenvi, N.; Roy, S.; Tully, J. C. Dynamical steering and electronic excitation in NO scattering from a gold surface. *Science* **2009**, *326*, 829–832.

(6) Alemani, M.; Peters, M. V.; Hecht, S.; Rieder, K.-H.; Moresco, F.; Grill, L. Electric field-induced isomerization of azobenzene by STM. *Journal of the American Chemical Society* **2006**, *128*, 14446–14447.

(7) Danilov, A. V.; Kubatkin, S. E.; Kafanov, S. G.; Flensberg, K.; Bjørnholm, T. Electron transfer dynamics of bistable single-molecule junctions. *Nano letters* **2006**, *6*, 2184–2190.

(8) Donarini, A.; Grifoni, M.; Richter, K. Dynamical symmetry breaking in transport through molecules. *Physical review letters* **2006**, *97*, 166801.

(9) Henningsen, N.; Franke, K.; Torrente, I.; Schulze, G.; Priewisch, B.; Rück-Braun, K.; Dokić, J.; Klamroth, T.; Saalfrank, P.; Pascual, J. Inducing the rotation of a single phenyl ring with tunneling electrons. *The Journal of Physical Chemistry C* **2007**, *111*, 14843–14848.

(10) Datta, S.; Tian, W.; Hong, S.; Reifenberger, R.; Henderson, J. I.; Kubiak, C. P. Current-voltage characteristics of self-assembled monolayers by scanning tunneling microscopy. *Physical Review Letters* **1997**, *79*, 2530.

(11) Samanta, M.; Tian, W.; Datta, S.; Henderson, J.; Kubiak, C. Electronic conduction through organic molecules. *Physical review B* **1996**, *53*, R7626.

(12) Nitzan, A.; Ratner, M. A. Electron transport in molecular wire junctions. *Science* **2003**, *300*, 1384–1389.

(13) Mujica, V.; Kemp, M.; Roitberg, A.; Ratner, M. Current-voltage characteristics of molecular wires: Eigenvalue staircase, Coulomb blockade, and rectification. *The Journal of chemical physics* **1996**, *104*, 7296–7305.

(14) Hsu, C.-P.; Marcus, R. A sequential formula for electronic coupling in long range bridge-assisted electron transfer: Formulation of theory and application to alkanethiol monolayers. *The Journal of chemical physics* **1997**, *106*, 584–598.

(15) Stipe, B. C.; Rezaei, M. A.; Ho, W. Single-molecule vibrational spectroscopy and microscopy. *Science* **1998**, *280*, 1732–1735.

(16) Marcus, R. A. On the theory of oxidation-reduction reactions involving electron transfer. I. *The Journal of chemical physics* **1956**, *24*, 966–978.

(17) Hush, N. S. Adiabatic theory of outer sphere electron-transfer reactions in solution. *Transactions of the Faraday Society* **1961**, *57*, 557–580.

(18) Levich, V. G.; Dogonadze, R. R. An adiabatic theory of electron processes in solutions. Doklady Akademii Nauk. 1960; pp 158–161.

(19) Cukier, R. I.; Nocera, D. G. Proton-coupled electron transfer. *Annual Review of Physical Chemistry* **1998**, *49*, 337–369.

(20) Jortner, J.; Bixon, M.; Langenbacher, T.; Michel-Beyerle, M. E. Charge transfer and transport in DNA. *Proceedings of the National Academy of Sciences* **1998**, *95*, 12759–12765.

(21) Morin, M.; Levinos, N.; Harris, A. Vibrational energy transfer of CO/Cu (100): Nonadiabatic vibration/electron coupling. *The Journal of Chemical Physics* **1992**, *96*, 3950–3956.

(22) Huang, Y.; Rettner, C. T.; Auerbach, D. J.; Wodtke, A. M. Vibrational promotion of electron transfer. *Science* **2000**, *290*, 111–114.

(23) Jiang, B.; Alducin, M.; Guo, H. Electron–hole pair effects in polyatomic dissociative chemisorption: Water on Ni (111). *The Journal of Physical Chemistry Letters* **2016**, *7*, 327–331.

(24) Persson, B.; Lang, N. Electron-hole-pair quenching of excited states near a metal. *Physical Review B* **1982**, *26*, 5409.

(25) De Jongh, P.; Vanmaekelbergh, D.; Kelly, J. J. d. Photoelectrochemistry of electrodeposited Cu2 O. *Journal of The Electrochemical Society* **2000**, *147*, 486.

(26) Hammes-Schiffer, S. Proton-coupled electron transfer: Moving together and charging forward. *Journal of the American Chemical Society* **2015**, *137*, 8860–8871.

(27) Marcus, R. On the theory of oxidation—reduction reactions involving electron transfer. v. comparison and properties of electrochemical and chemical rate constants1. *The Journal of Physical Chemistry* **1963**, *67*, 853–857.

(28) Dou, W.; Subotnik, J. E. Nonadiabatic Molecular Dynamics at Metal Surfaces. *The Journal of Physical Chemistry A* **2020**, *124*, 757–771.

(29) Shenvi, N.; Roy, S.; Tully, J. C. Nonadiabatic dynamics at metal surfaces: Independent-electron surface hopping. *The Journal of Chemical Physics* **2009**, *130*, 174107.

(30) Dou, W.; Subotnik, J. E. A broadened classical master equation approach for nonadiabatic dynamics at metal surfaces: Beyond the weak molecule-metal coupling limit. *The Journal of Chemical Physics* **2016**, *144*, 024116.

(31) Jin, Z.; Subotnik, J. E. Nonadiabatic dynamics at metal surfaces: fewest switches surface hopping with electronic relaxation. *Journal of Chemical Theory and Computation* **2021**, *17*, 614–626.

(32) Hedin, L. New method for calculating the one-particle Green's function with application to the electron-gas problem. *Physical Review* **1965**, *139*, A796.

(33) Onida, G.; Reining, L.; Rubio, A. Electronic excitations: density-functional versus many-body Green's-function approaches. *Reviews of modern physics* **2002**, *74*, 601.

(34) Liu, Z.-F.; da Jornada, F. H.; Louie, S. G.; Neaton, J. B. Accelerating GW-based energy level alignment calculations for molecule–metal interfaces using a substrate screening approach. *Journal of Chemical Theory and Computation* **2019**, *15*, 4218–4227.

(35) Klüner, T.; Govind, N.; Wang, Y. A.; Carter, E. A. Periodic density functional embedding theory for complete active space self-consistent field and configuration interaction calculations: Ground and excited states. *The Journal of chemical physics* **2002**, *116*, 42–54.

(36) Lahav, D.; Klüner, T. A self-consistent density based embedding scheme applied to the adsorption of CO on Pd (111). *Journal of Physics: Condensed Matter* **2007**, *19*, 226001.

(37) Mehdaoui, I.; Klüner, T. Understanding surface photochemistry from first principles: The case of CO-NiO (100). *Physical review letters* **2007**, *98*, 037601.

(38) Martirez, J. M. P.; Carter, E. A. Prediction of a low-temperature N2 dissociation cat-

alyst exploiting near-IR–to–visible light nanoplasmonics. *Science advances* **2017**, *3*, eaao4710.

(39) Wu, Q.; Van Voorhis, T. Extracting electron transfer coupling elements from constrained density functional theory. *The Journal of chemical physics* **2006**, *125*, 164105.

(40) Wu, Q.; Van Voorhis, T. Direct optimization method to study constrained systems within density-functional theory. *Physical Review A* **2005**, *72*, 024502.

(41) Behler, J.; Delley, B.; Reuter, K.; Scheffler, M. Nonadiabatic potential-energy surfaces by constrained density-functional theory. *Physical Review B* **2007**, *75*, 115409.

(42) Kaduk, B.; Kowalczyk, T.; Van Voorhis, T. Constrained density functional theory. *Chemical Reviews* **2012**, *112*, 321–370.

(43) Meng, G.; Jiang, B. A pragmatic protocol for determining charge transfer states of molecules at metal surfaces by constrained density functional theory. *The Journal of Chemical Physics* **2022**, *157*, 214103.

(44) Goldey, M. B.; Brawand, N. P.; Voros, M.; Galli, G. Charge transport in nanostructured materials: implementation and verification of constrained density functional theory. *Journal of chemical theory and computation* **2017**, *13*, 2581–2590.

(45) Ma, H.; Wang, W.; Kim, S.; Cheng, M.-H.; Govoni, M.; Galli, G. PyCDFT: A Python package for constrained density functional theory. *Journal of Computational Chemistry* **2020**,

(46) Souza, A.; Rungger, I.; Pemmaraju, C.; Schwingenschlögl, U.; Sanvito, S. Constrained-DFT method for accurate energy-level alignment of metal/molecule interfaces. *Physical Review B* **2013**, *88*, 165112.

(47) Gavnholt, J.; Olsen, T.; Engelund, M.; Schiøtz, J. Δ self-consistent field method to

obtain potential energy surfaces of excited molecules on surfaces. *Physical Review B* **2008**, *78*, 075441.

(48) Chen, J.; Subotnik, J. (unpublished).

(49) Helgaker, T.; Jorgensen, P.; Olsen, J. *Molecular electronic-structure theory*; John Wiley & Sons, 2013.

(50) Battaglia, S.; Lindh, R. Extended dynamically weighted CASPT2: The best of two worlds. *Journal of chemical theory and computation* **2020**, *16*, 1555–1567.

(51) Wright, S.; Nocedal, J., et al. Numerical optimization. *Springer Science* **1999**, *35*, 7.

(52) For the specific case of one site model, there is no reason to solve the Newton-KKT equations because we can actually force the first active orbital to be fully localized on the impurity, and therefore the second active orbital must be a pure bath orbital due to orthogonality. In such a case, the Newton-KKT constraint is automatically satisfied.

(53) Glover, W. Communication: Smoothing out excited-state dynamics: Analytical gradients for dynamically weighted complete active space self-consistent field. *The Journal of Chemical Physics* **2014**, *141*, 171102.

(54) Gagliardi, L.; Truhlar, D. G.; Li Manni, G.; Carlson, R. K.; Hoyer, C. E.; Bao, J. L. Multiconfiguration pair-density functional theory: A new way to treat strongly correlated systems. *Accounts of chemical research* **2017**, *50*, 66–73.

(55) Athavale, V.; Teh, H.-H.; Shao, Y.; Subotnik, J. Analytical gradients and derivative couplings for the TDDFT-1D method. *The Journal of Chemical Physics* **2022**, *157*, 244110.

(56) Bannwarth, C.; Yu, J. K.; Hohenstein, E. G.; Martínez, T. J. Hole–hole Tamm–Dancoff-approximated density functional theory: A highly efficient electronic structure method

incorporating dynamic and static correlation. *The Journal of Chemical Physics* **2020**, *153*, 024110.

TOC Graphic

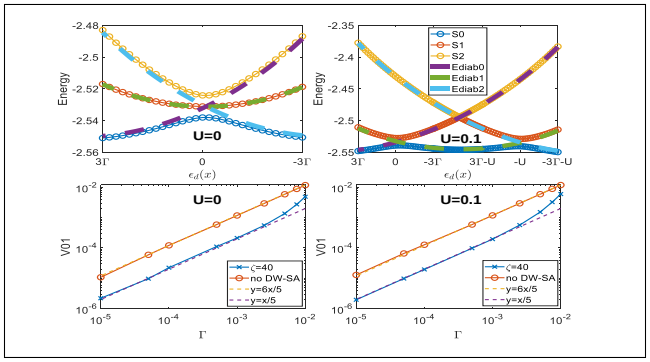
Energy
U=0
U=0.1
S0
S1
S2
Ediab0
Ediab1
Ediab2
$\epsilon_d(x)$
V01
Γ
ζ=40
no DW-SA
y=6x/5
y=x/5